Check for updates

*International Journal of Energy Research*

WILEY

RESEARCH ARTICLE OPEN ACCESS

# Grid-Constrained Sizing and Predictive Dispatch of a PV–Battery–Hydrogen Energy Community: An Island Case Study

Abdelaziz Abualshawareb[1] | Zahir Dehouche[1] | Carola S. König[1] | Ximena Schmidt Rivera[2] | Sergi Ribas[3] | Ioana Pisica[4]

[1]Department of Mechanical and Aerospace Engineering, College of Engineering, Design and Physical Sciences, Brunel University of London, Uxbridge, UB8 3PH, UK | [2]Department of Chemical Engineering, College of Engineering, Design and Physical Sciences, Brunel University of London, Uxbridge, UB8 3PH, UK | [3]Activities and Operations, Island Council of Formentera, Pius Tur Mayans Street, 14, Sant Francesc 07860, Formentera, Spain | [4]Department of Electronic and Electrical Engineering, College of Engineering, Design and Physical Sciences, Brunel University of London, Uxbridge, UB8 3PH, UK

**Correspondence:** Ioana Pisica (ioana.pisica@brunel.ac.uk)

**Received:** 3 February 2026 | **Revised:** 5 August 2026 | **Accepted:** 14 August 2026

## ABSTRACT

Grid-connected energy communities on weak or capacity-limited feeders increasingly consider hybrid photovoltaic (PV)–battery–hydrogen systems yet planning studies often size assets against annual balances while leaving the grid connection as an effectively unconstrained buffer. Here, we develop a boundary-centred planning architecture that couples long-horizon investment decisions to schedule-feasible operation. A genetic algorithm (GA) selects component capacities, inverter rating, and contracted import/export power, while a rolling-horizon (MILP) formulation implements model predictive control (MPC) resolves tariff-coupled dispatch with bounded daily load shifting. Using a public-sector community on the island of Formentera (Spain), we benchmark reactive load-following against predictive operation under 0% to 8% flexible demand. Predictive coordination reshapes both, sizing and energy flows by converting temporal foresight into "capacity value" at the point of common coupling. Relative to load-following, the optimiser tightens the contracted exchange envelope from ±78 to ±37 kW and reduces the inverter rating from 120 to 77 kW, while increasing PV utilisation and reducing grid import reliance to roughly 9%–11% of demand. These gains arise from coordinated storage operation: the battery provides mostly short-term balancing, while hydrogen supplies a smaller secondary contribution through surplus absorption and occasional deficit support. Economically, modest flexibility amplifies the effect, reducing net present cost (NPC) by 9% and lowering levelised electricity cost (LCOE) from 0.243 to 0.218 €/kWh. Together, the results show that hybrid community value is anchored in enforceable boundary control, and that limited behavioural adaptation can substitute for contracted capacity in weak-grid planning.

## 1 | Introduction

Islands and other weak-grid communities face structural constraints that can be more binding than in strongly interconnected systems, including limited interconnection capacity, high reinforcement costs, and strong intra-annual variability in demand and resource availability [1]. In Europe alone, more than sixteen million people live on islands, making them a focal point for the European Commission's Clean Energy for EU Islands initiative [2]. Electricity generation costs can reach several times mainland averages [3], reflecting dependence on imported fuels and constrained infrastructure. These conditions make island and weak-grid planning not simply a matter of resource potential but one of coordinating variable generation with constrained grid interfaces,

This is an open access article under the terms of the Creative Commons Attribution License, which permits use, distribution and reproduction in any medium, provided the original work is properly cited.

Copyright © 2026 Abdelaziz Abualshawareb et al. *International Journal of Energy Research* published by John Wiley & Sons Ltd.

where limited import and export capacity at the grid connection point defines feasible operation [4]. In such contexts, the planning bottleneck is often the magnitude of net power exchange at the grid connection point, since high import peaks and export surges can drive curtailment, increase demand-related charges, and motivate higher contracted capacities or network reinforcement [5, 6]. Hybrid battery–hydrogen systems are increasingly investigated as a means to combine diurnal and long-duration flexibility [7]. Together, these conditions expose a persistent methodological challenge, linking long-term capacity investment with operational feasibility under tariff and grid-exchange constraints, a question that recent research has approached from multiple methodological directions.

Recent reviews have examined sizing optimisation of off-grid hybrid renewable energy systems for remote and island communities [8], showing that reliable renewable supply depends not only on resource availability but also on the mismatch between renewable output and the load profile as well as the adequacy of energy storage [8]. However, most of the reviewed studies relied on rule-based energy management and heuristic sizing approaches highlighting the limited prevalence of integrated, operation-aware design tools. A structured systematic review extended this critique, identifying recurring challenges in island energy modelling including land scarcity, climatic exposure, pronounced annual variation in demand, isolation and remoteness, data scarcity, and socio-political and funding constraints [9]. They emphasised that many models still adopt single-year formulations at hourly resolution and often simplify grid interaction assumptions. Other studies noted that in hydrogen-based microgrids, the grid is commonly modelled as an effectively unlimited source or sink, while forecasting and constrained power exchange are seldom incorporated into energy management systems [10]. Similar conclusions were reported in systematic reviews of hybrid renewable energy systems with hydrogen storage, highlighting that component sizing and energy management are often treated separately and that rule-based energy management remains prevalent in the literature [11]. Together, these studies demonstrate that while island systems are well motivated, modelling practice can remain detached from the physical and economic constraints that determine feasibility in operation. Table 1 synthesises the reviewed studies and highlights, across grid and island contexts, which combinations of sizing, dispatch, tariff modelling, grid connection point constraints, and flexibility mechanisms have been implemented.

A growing body of work links long-term sizing with short-term operation. Zhang et al. [12] compared battery and hydrogen storage using genetic algorithm (GA)-based sizing and rule-based operation but without look-ahead scheduling. More recent frameworks incorporate predictive dispatch within sizing. Rullo et al. [14] coupled GA sizing with MILP-based economic model predictive control (MPC) and reported reductions in both investment and operating costs. Mohseni and Brent [15] extended the scheduling horizon from 24 to 72 h, reducing whole-life cost by up to 8%. Al-Quraan and Al-Mhairat [16] similarly embedded receding-horizon economic MPC within bi-level sizing, although the operational assessment was restricted to selected periods. These studies demonstrate the value of predictive dispatch but retain trade-offs between temporal coverage, computational burden, and representation of grid-interface constraints.

Weak-grid planning also needs a clearer structural model at the point of connection, where the inverter rating and contracted import/export limits jointly bound power exchange. Prior work shows that tighter contracted capacity can increase self-consumption but raises lifecycle cost [17], yet treats contract level as exogenous. Others optimise import/export capacities as sizing variables [18] but retain deterministic dispatch and limited tariff coupling. Tariff-driven scheduling has been studied under ToU and demand charges [19] and inverter sizing/DC–AC ratio effects under ToU [20], but under weak-grid conditions inverter rating is a physical constraint interacting with contracted limits and penalties. The literature rarely co-optimises inverter and contracted power within an operationally feasible predictive framework.

A further gap is behavioural flexibility. ToU tariffs affect storage cycling and grid exchanges [21], but demand is typically fixed. Continuous price-responsive demand models [22] are poorly suited to small communities where flexibility comes from discrete, schedulable devices. More practical bounded-deferral and demand-response formulations show that modest deferrable load can reduce required battery capacity and cost [23–26], yet this flexibility is often only loosely coupled to tariff-driven, grid-constrained predictive dispatch. Integrating enforceable modest flexibility with receding-horizon operation under contracted exchange limits remains open.

Storage coordination of hybrids such as battery and hydrogen is well motivated but still operationally underdeveloped for grid-constrained communities. Detailed MILP planning for power-to-hydrogen resolves component sizing and hourly grid trades with realistic electrolyser behaviour [27] but assumes full-year foresight and often omits explicit exchange limits. Comparative studies show hybrids exploit complementary time scales—batteries for short cycles and hydrogen for longer-duration energy shifting, such as improving self-sufficiency and cost [28], yet operation is frequently strategy-based, and grid-interface constraints are simplified.

Taken together, unresolved gaps are intertwined: temporal (foresight vs. representativeness), structural (inverter and contracted exchange limits), behavioural (bounded device flexibility), and multi-vector coordination. Bridging them requires a framework that unifies long-horizon sizing with sequential, predictive dispatch under explicit point-of-connection constraints and realistic tariff/contract coupling.

This paper proposes an integrated planning framework for grid-connected PV–battery–hydrogen communities on constrained or weak grids. The framework unites long-horizon capacity sizing with short-horizon predictive dispatch under ToU tariffs, treating inverter rating and contracted grid power as co-optimised decision variables and incorporating modest flexible load participation to reduce peak exchanges and enhance economic performance. As shown in Figure 1, the system comprises interconnected AC and DC buses. PV generation, the battery and fuel cell are connected to the DC bus, while the community demand, grid connection and electrolyser are represented on the AC side. For clarity, Figure 1 presents the system-level electrical connections: the electrolyser is treated as an AC-coupled unit with internal rectification, while the fuel cell is represented by its DC connection to the DC bus, without detailing the internal power electronics. A shared inverter couples the two buses and constrains power transfer between the



ijer, 2026, 1, Downloaded from https://onlinelibrary.wiley.com/doi/10.1155/er/5550759 by NICE, National Institute for Health and Care Excellence, Wiley Online Library on [08/11/2026]. See the Terms and Conditions (https://onlinelibrary.wiley.com/terms-and-conditions) on Wiley Online Library for rules of use; OA articles are governed by the applicable Creative Commons License

**TABLE 1** | Comparison of optimisation references, showing grid/island context, and which advanced features are implemented.

| Reference | Grid/island | System structure | Method features | | | | | | | | | | Remarks |
|---|---|---|---|---|---|---|---|---|---|---|---|---|---|
| | | | GS | DO | RH | SH | LS | CG | IC | AD | TO | PS | |
| [12] | Grid | PV-BT or PV-EL-TK-FC | ✓ | ✓ | ✗ | ✓ | ✗ | ✗ | ✗ | ✓ | ✓ | ✓ | GA-based sizing; operation evaluated using LP solved per time step within rule-based strategies; includes an explicit peak-shaving objective and revenue terms. |
| [13] | Grid | PV-BT-EL-TK-FC | ✗ | ✓ | ✗ | ✓ | ✗ | ✗ | ✗ | ✗ | ✓ | ✗ | Year-long MILP using clustered (typical) design days; includes power-to-gas and hydrogen storage; assumes spot-price electricity and feed-in tariff for exports. |
| [14] | Off grid | PV-WT-BT-EL-TK-FC | ✓ | ✓ | ✓ | ✗ | ✗ | ✗ | ✗ | ✓ | ✗ | ✗ | Bi-level GA sizing with a MILP-based economic MPC energy manager (rolling horizon); assumes perfect information knowledge of the predictive layer. |
| [15] | Grid | PV-WT-BT | ✓ | ✓ | ✓ | ✗ | ✗ | ✗ | ✓ | ✓ | ✓ | ✗ | Metaheuristic sizing with LP dispatch over a moving multi-day scheduling window; uses spot-price import and feed-in tariff export vectors; inverter rating is a sizing variable. |
| [16] | Grid | PV-WT-BT-EL-TK-FC | ✓ | ✓ | ✓ | ✗ | ✗ | ✗ | ✗ | ✓ | ✗ | ✗ | Bi-level multi-objective GA sizing; economic MPC dispatch applies receding-horizon optimisation with only the first control move implemented each step; grid price is a constant buy and sell tariff. |
| [17] | Grid/Off-Grid | PV–BT | ✗ | ✓ | ✗ | ✓ | ✗ | ✗ | ✓ | ✓ | ✓ | ✓ | Multi-objective MILP with full-year hourly resolution; analyses peak shaving through subscription-limit scenarios; converter ratings are optimised design variables. |
| [18] | Grid | PV–FC–EL–TK-INV | ✓ | ✗ | ✗ | ✓ | ✗ | ✓ | ✗ | ✓ | ✗ | ✗ | Metaheuristic sizing with rule-based operational strategy; grid import and export capacity limits are treated as design variables; buy and sell prices are constant scalars. |
| [19] | Grid | PV–BT | ✗ | ✓ | ✗ | ✓ | ✗ | ✗ | ✗ | ✓ | ✓ | ✓ | MILP-based sizing and MILP energy scheduling under ToU energy tariffs and demand charges; demand charges drive peak-shaving behaviour. |
| [20] | Grid | PV–BT-INV | ✗ | ✗ | ✗ | ✓ | ✗ | ✗ | ✗ | ✓ | ✓ | ✓ | Fixed dispatch schedule designed and evaluated in SAM; focuses on PV clipping utilisation and peak-load reduction under ToU; does not optimise dispatch. |
| [21] | Grid | PV–WT–BT–EL–TK–FC | ✓ | ✗ | ✗ | ✓ | ✗ | ✗ | ✗ | ✗ | ✓ | ✓ | LSC-SSA metaheuristic sizing with rule-based energy management; includes fixed grid exchange limits; uses ToU peak-hour logic in the energy management rules. |
| [22] | Off grid | PV-WT–EL–TK–FC | ✓ | ✓ | ✗ | ✓ | ✓ | ✗ | ✗ | ✗ | ✓ | ✓ | Bi-level optimisation: CS-PSO for sizing and NSGA-II for operation and demand response tariff tuning; uses clustered typical scenarios; dispatch variables are optimised per time step. |
| [23] | Off grid | PV–BT and PV–BT–DG | ✓ | ✗ | ✗ | ✓ | ✓ | ✗ | ✗ | ✗ | ✗ | ✓ | PSO sizing with rule-based priority load shifting (high- and low-priority loads) allowing up to 24 h deferral; ToU is mentioned as a possible application but not modelled as a tariff. |
| [24] | Off grid | PV–WT–PHES | ✓ | ✗ | ✗ | ✓ | ✓ | ✗ | ✗ | ✗ | ✓ | ✓ | Three-step planning for an isolated microgrid; uncertainty handled using Latin hypercube sampling, *k*-means clustering, and Monte Carlo simulation; sizing solved via GA; operation uses feasibility checks and demand response incentives rather than an optimisation-based scheduler. |

(Continues)



iler, 2026, 1, Downloaded from https://onlinelibrary.wiley.com/doi/10.1155/er/5550759 by NICE, National Institute for Health and Care Excellence, Wiley Online Library on [08/1/2026]. See the Terms and Conditions (https://onlinelibrary.wiley.com/terms-and-conditions) on Wiley Online Library for rules of use; OA articles are governed by the applicable Creative Commons License

**TABLE 1** | (Continued)

| Reference | Grid/island | System structure | Method features | | | | | | | | | Remarks |
|---|---|---|---|---|---|---|---|---|---|---|---|---|
| | | | GS | DO | RH | SH | LS | CG | IC | AD | TO | PS | |
| [25] | Off grid | PV–BT–EL–TK–FC | ✗ | ✓ | ✗ | ✓ | ✓ | ✗ | ✗ | ✓ | ✓ | ✗ | Single-layer MILP co-optimises design and full-year hourly scheduling; uses piecewise-affine component performance curves; includes a ToU -based demand response programme that shifts load within a daily horizon. |
| [26] | Off grid | PV–WT–BT–INV | ✓ | ✗ | ✗ | ✓ | ✓ | ✗ | ✓ | ✓ | ✗ | ✓ | Metaheuristic sizing with integrated direct load control demand response; time-series compressed from 8760 h to representative points; inverter rating is a sizing variable; demand response reduces peaks. |
| [27] | Grid | PV–BT–EL–TK | ✗ | ✓ | ✗ | ✓ | ✗ | ✗ | ✗ | ✗ | ✓ | ✗ | MILP co-optimises sizing and full-year hourly operation; includes explicit grid buy and sell power variables and piecewise-affine electrolyser efficiency; no explicit grid exchange capacity (contract) limit is imposed. |
| [28] | Grid | PV–BT/PV–BT–EL–TK–FC | ✓ | ✗ | ✗ | ✓ | ✗ | ✗ | ✗ | ✗ | ✓ | ✗ | A metaheuristic searches component sizes and operational strategy parameters; operation is simulated using rule-based strategies (CS and OLDS) over 8760 h; uses ToU electricity prices (peak, shoulder, off-peak) |
| This work | Grid | PV-BT-EL-TK-FC-INV | ✓ | ✓ | ✓ | ✓ | ✓ | ✓ | ✓ | ✓ | ✓ | ✓ | GA-based sizing combined with day-ahead MILP scheduling and an MPC (12-h horizon); co-optimises contracted grid limits and inverter rating; explicit AC/DC topology; includes ToU tariffs, peak-shaving mechanisms, and bounded load shifting. |

Abbreviations: AD, detailed AC/DC buses; CG, contracted-grid optimisation; DO, dispatch optimisation; GS, meta-heuristic sizing; IC, inverter-capacity optimisation; LS, load-shifting; PS, peak-shaving; RH, rolling-horizon/MPC; SH, static-hourly assumption; TO, time-of-use tariffs.

renewable and storage assets and the point of common coupling. The electrolyser and fuel cell provide the electrical-to-hydrogen and hydrogen-to-electrical conversion pathways, respectively. Accordingly, the framework provides a planning-stage techno-economic assessment in which weak-grid conditions are represented by finite contracted import and export capacity at the point of common coupling, together with the inverter throughput limit; this assessment can be complemented by network-quality, environmental and stakeholder criteria during detailed project development. The following sections describe the optimisation framework, present a case study for a public-sector energy community on Formentera Island, and benchmark the proposed strategy against rule-based load-following baselines.

## 2 | Methodology

The proposed optimisation framework integrates a hierarchical control architecture that combines long-term capacity sizing with short-horizon dispatch optimisation under operational and contractual constraints. As shown in Figure 2, the framework couples a GA with a rolling-horizon MILP model to minimise the system's net present cost (NPC) over a 1-year horizon. The GA serves as the global loop, exploring candidate system configurations across photovoltaic (PV) capacity, battery storage, inverter rating, hydrogen subsystems, and grid exchange limits. Each configuration is passed to the local loop, where dispatch is resolved using a 24-h receding horizon structure that emulates MPC. This formulation enables tariff-driven scheduling, bounded load flexibility, and coordinated battery–hydrogen storage operation, while enforcing feasibility under inverter and contracted grid constraints. The following sections formalise the sizing variables, objective function, and predictive dispatch logic underpinning this layered optimisation strategy.

### 2.1 | GA-Global Loop for Capacity Sizing

The global layer of the proposed framework employs a GA to explore optimal capacity allocations for hybrid renewable systems. Its objective is to minimise the system's NPC by iteratively evaluating candidate configurations over the planning horizon. Each candidate solution represents a complete system design defined by a vector of decision variables that describe the installed capacities of the main subsystems. These capacities govern both, investment requirements and the operational feasibility of dispatch at the lower MILP level. Formally, each GA individual is expressed as:

$$\boldsymbol{x} = \left[\overline{P}_{\mathrm{pv}}, \overline{N}_{\mathrm{bat}}, \overline{P}_{\mathrm{inv}}, \overline{P}_{\mathrm{gr}}, \overline{P}_{\mathrm{fc}}, \overline{P}_{\mathrm{el}}, \overline{M}_{\mathrm{H_2}}\right]. \tag{1}$$

Here where $\overline{P}_{\mathrm{pv}}$ is the installed PV capacity (kW), $\overline{N}_{\mathrm{bat}}$ is the number of battery modules, and $\overline{P}_{\mathrm{inv}}$ denotes the inverter rating (kW). The term $\overline{P}_{\mathrm{gr}}$ represents the contracted grid exchange limit (kW), while $\overline{P}_{\mathrm{fc}}$ and $\overline{P}_{\mathrm{el}}$ correspond to the nominal power ratings of the fuel cell and electrolyser, respectively. Finally, $\overline{M}_{\mathrm{H_2}}$ specifies the hydrogen storage capacity (kg). This vector encodes both DC and AC subsystem components, enabling the GA to evolve feasible topologies under investment and operational constraints. For each configuration $\boldsymbol{x}$, the NPC aggregates capital $C_{k,y}$, replacement $R_{k,y}$, operating $O_y$, and salvage costs $S_{k,y}$ over the system lifetime $Y$, discounted by the real interest rate $i$:



ijer, 2026, 1, Downloaded from https://onlinelibrary.wiley.com/doi/10.1155/er/5550739 by NICE, National Institute for Health and Care Excellence, Wiley Online Library on [08/11/2026]. See the Terms and Conditions (https://onlinelibrary.wiley.com/terms-and-conditions) on Wiley Online Library for rules of use; OA articles are governed by the applicable Creative Commons License

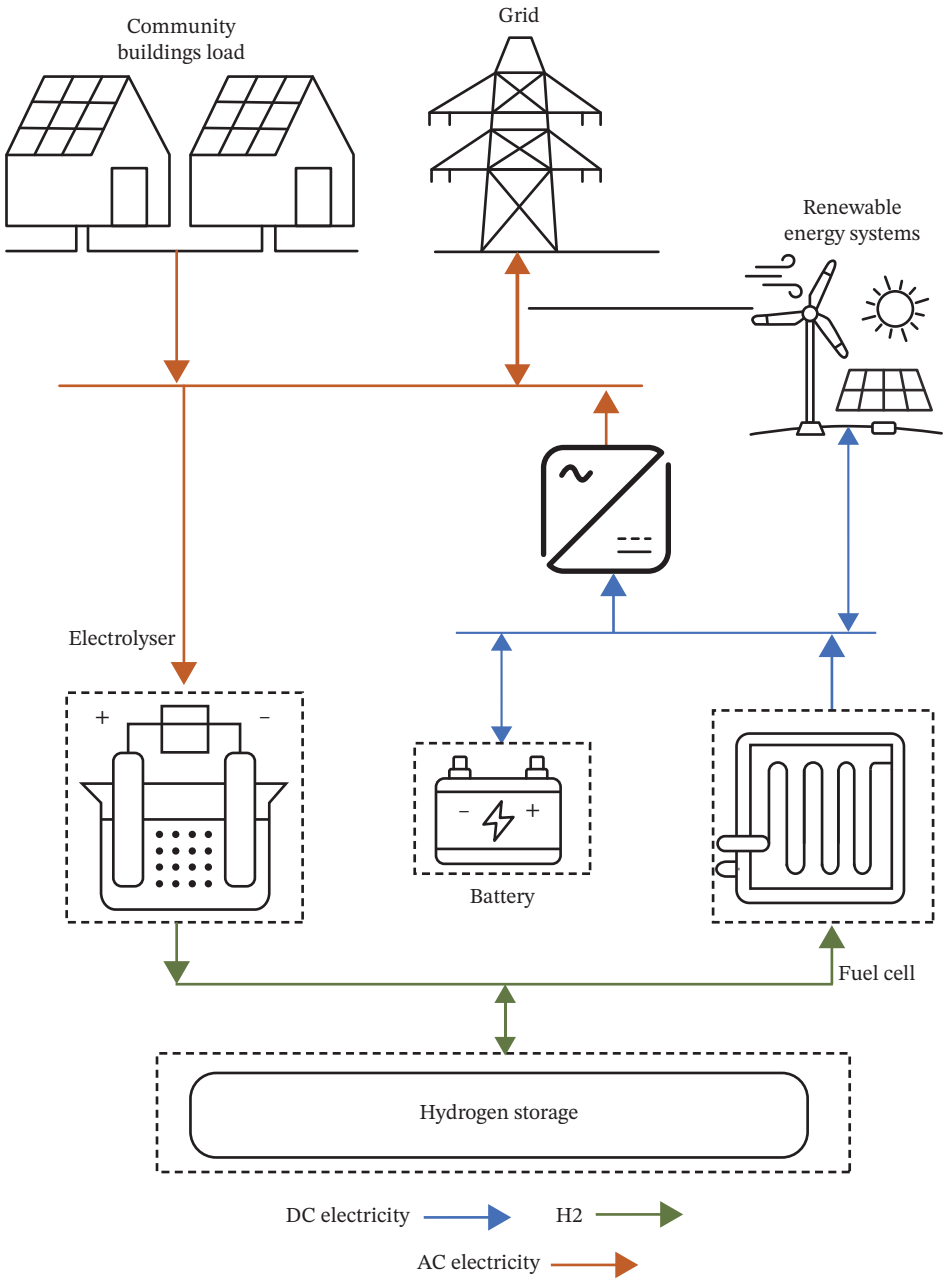



**FIGURE 1** | System layout for the grid-connected PV–battery–hydrogen energy community.

$$\min_{\boldsymbol{x}\in\mathcal{X}} \mathrm{NPC}(\boldsymbol{x}) = \sum_{y=0}^{Y} \frac{1}{(1+i)^y} \left[ \sum_{k\in\mathcal{K}} \left( C_{k,y}(\boldsymbol{x}) + R_{k,y}(\boldsymbol{x}) - S_{k,y}(\boldsymbol{x}) \right) + O_y(\boldsymbol{x}) \right]. \tag{2}$$

This fitness function captures both investment efficiency and operational performance, allowing the GA to evolve towards economically and technically viable configurations. The framework was implemented in Python, using DEAP for the GA and Gurobi solver for the rolling-horizon MILP evaluations. The configuration used for the final GA–MPC optimisation is reported in Table 2.

Candidate evaluations were parallelised. Convergence was monitored using the lowest NPC in each generation; the best generational value changed by less than 0.02% over the final 10 generations, indicating practical stabilisation before termination. To evaluate PV production profiles, the framework uses a temperature-adjusted irradiance model that reflects hourly variations in solar resource and thermal conditions:

$$P_t^{\mathrm{PV}} = \overline{P}_{\mathrm{pv}} \cdot \eta_{\mathrm{der}} \cdot \frac{G_t}{G^{\mathrm{STC}}} \cdot [1 + \alpha(T_t - T^{\mathrm{STC}})], \tag{3}$$

where $\eta_{\mathrm{der}}$ is the PV derating factor accounting for system losses, $G_t$ is the incident irradiance, $G^{\mathrm{STC}}$ is the standard irradiance ($1\,\mathrm{kW/m^2}$), $\alpha$ is the temperature coefficient, and $T_t$ and $T^{\mathrm{STC}}$ denote the cell temperature at time $t$ and under standard test conditions, respectively. This formulation ensures that intra-annual and daily variations in PV yield are consistently propagated to the dispatch model and cost evaluation.



ijer, 2026, 1, Downloaded from https://onlinelibrary.wiley.com/doi/10.1155/er/5550739 by NICE, National Institute for Health and Care Excellence, Wiley Online Library on [08/11/2026]. See the Terms and Conditions (https://onlinelibrary.wiley.com/terms-and-conditions) on Wiley Online Library for rules of use; OA articles are governed by the applicable Creative Commons License

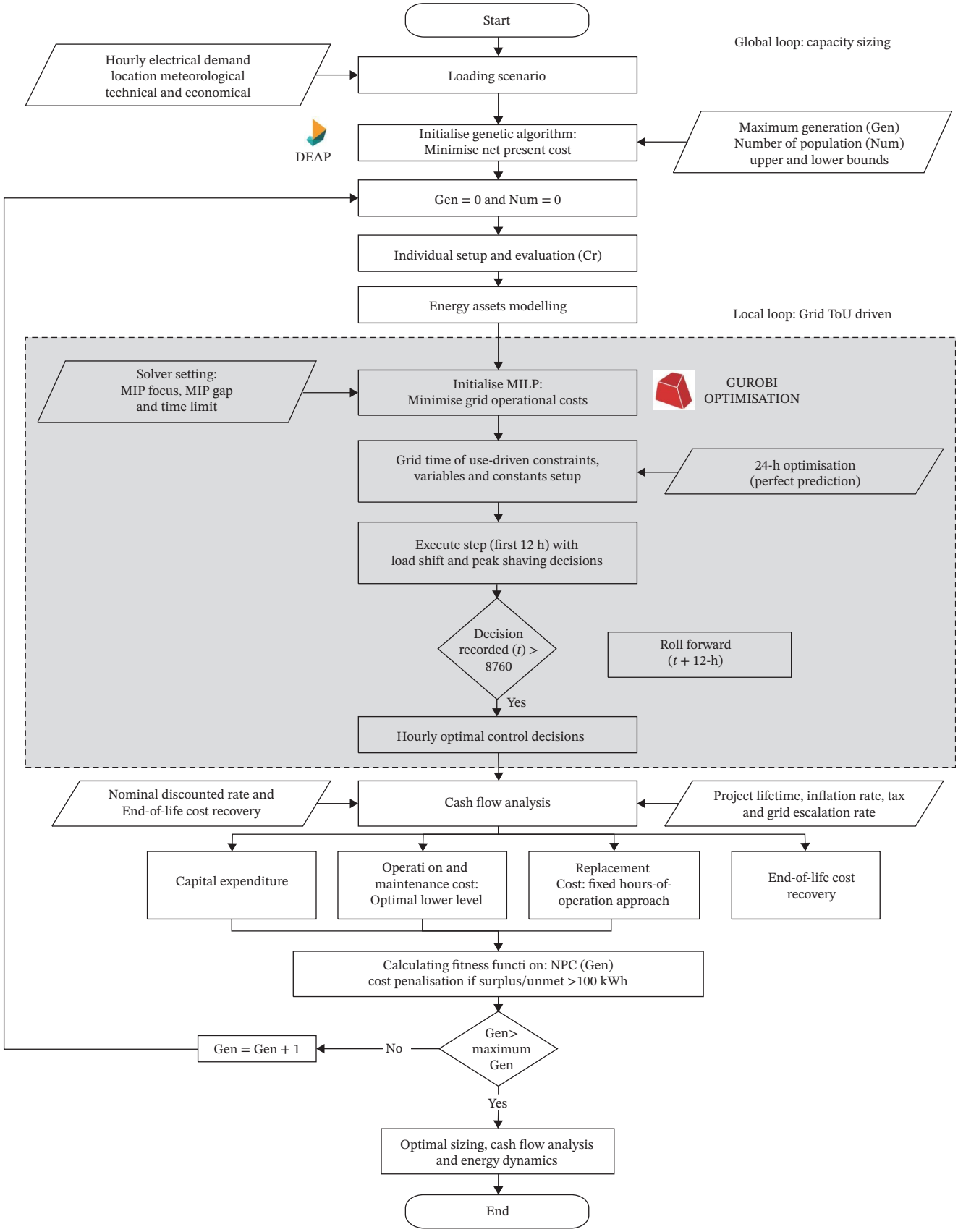



**FIGURE 2** | Bi-level optimisation framework combining GA-based capacity sizing with MILP-based rolling-horizon dispatch under ToU tariffs and grid constraints.



ijer, 2026, 1, Downloaded from https://onlinelibrary.wiley.com/doi/10.1155/er/5550759 by NICE, National Institute for Health and Care Excellence, Wiley Online Library on [08/11/2026]. See the Terms and Conditions (https://onlinelibrary.wiley.com/terms-and-conditions) on Wiley Online Library for rules of use; OA articles are governed by the applicable Creative Commons License

**TABLE 2** | GA configuration for the final GA–MPC 8% optimisation.

| Parameter | Setting |
|---|---|
| Population size | 120 |
| Number of generations | 70 |
| Mutation probability | 0.4 |
| Crossover probability | 0.7 |
| Recorded wall-clock time | 3 h 36 min |

To discourage designs that cause persistent energy imbalance, either through frequent curtailment or unmet demand, a penalty term is added to the objective function. The penalty activates only when cumulative annual energy imbalance exceeds a defined tolerance ε:

$$\Phi = \begin{cases} \Phi_{\text{ex/un}}, & \text{if } \sum_{t\in T} E_{\text{ex/un}}(t) > \varepsilon \\ 0, & \text{otherwise} \end{cases}. \tag{4}$$

Here, $E_{\text{ex/un}}(t)$ is the cumulative annual excess or unmet energy, $\varepsilon$ is the corresponding tolerance (e.g., 100 kWh year$^{-1}$), and $\Phi_{\text{ex/un}}$ is the fixed penalty applied when that tolerance is exceeded. Since $\Phi_{\text{ex/un}}$ enters the NPC objective directly, its unit is Euros (€). This formulation enhances the robustness of selected designs by embedding system reliability directly into the economic objective, particularly for weak-grid or islanded operation where energy balance is critical.

## 2.2 | MILP- Local Dispatch Loop

Once a candidate system configuration **x** is selected by the GA, it is evaluated within the local dispatch layer. This layer uses a MILP formulation to optimise hourly scheduling of renewable generation, grid exchanges, storage behaviour, and hydrogen subsystem operation under ToU tariffs. To ensure temporal realism without prohibitive computational cost, the MILP is implemented as a rolling-horizon structure, in which each optimisation window represents a 24-h predictive horizon with a 12-h overlap between successive runs. For each window $w$, the optimisation considers the following time set:

$$\mathcal{T}_w = \{t_w, t_w + 1, \ldots, t_w + 23\}, \tag{5}$$

where $t_w$ is defined as the first hour of window $w$, computed recursively as:

$$t_w = t_0 + 12(w - 1). \tag{6}$$

Here, $t_0$ represents the simulation start time. Only the first half of each window's solution is committed to the final schedule, while the remaining portion is re-optimised in the next iteration, thereby emulating a receding-horizon predictive control logic. The objective of the MILP in each window is to minimise short-term operating costs, accounting for electricity imports, exports, curtailment, and unmet load penalties:

$$\min \sum_{t\in\mathcal{T}_w} \Delta t \cdot \left(\pi_t^{\text{imp}} P_t^{\text{imp}} - \pi_t^{\text{exp}} P_t^{\text{exp}} + \lambda^{\text{un}} P_t^{\text{un}} + \lambda^{\text{cur}} P_t^{\text{cur}}\right), \tag{7}$$

where $\pi_t^{\text{imp}}$ and $\pi_t^{\text{exp}}$ are the import and export tariffs (€/kWh) at time $t$; $P_t^{\text{imp}}$ and $P_t^{\text{exp}}$ are the corresponding grid power flows; and $P_t^{\text{un}}$, $P_t^{\text{cur}}$ represent unmet demand and curtailed renewable generation, penalised by coefficients (€/kWh) $\lambda^{\text{un}}$ and $\lambda^{\text{cur}}$, respectively. Following common practice, a weighting ratio of ~10:1 is applied between unmet demand and curtailment to ensure supply reliability remains the dominant operational objective [14]. Operational feasibility within each rolling-horizon window is governed by a set of power-balance and exclusivity constraints that ensure energy conservation and physically valid scheduling across subsystems. The model distinguishes between the DC and AC domains, which are coupled through the central inverter. The DC-side energy balance ensures that, at each hour, all PV output, storage activity, and fuel cell production are correctly distributed between local use, conversion to AC power, and curtailed surplus:

$$P_t^{\text{PV,AC}} + P_t^{\text{PV,DC}} + P_t^{\text{dis}} + P_t^{\text{FC}} - P_t^{\text{ch}} - \frac{1}{\eta^{\text{inv}}} \cdot P_t^{\text{inv}} - P_t^{\text{cur}} = 0\,, \forall t \in \mathcal{T}. \tag{8}$$

Here, $P_t^{\text{PV,AC}}$ and $P_t^{\text{PV,DC}}$ denote the PV power routed to the AC and DC buses, respectively; $P_t^{\text{dis}}$ and $P_t^{\text{ch}}$ are the battery discharging and charging powers; $P_t^{\text{FC}}$ is the fuel-cell output; $P_t^{\text{inv}}$ is the DC-to-AC inverter throughput; and $\eta^{\text{inv}}$ is the inverter efficiency. The curtailed power $P_t^{\text{cur}}$ represents unused renewable generation at time $t$. The AC-side balance ensures that the sum of AC generation, grid exchanges, and hydrogen conversion processes meets the total demand, accounting for both fixed and flexible load components:

$$P_t^{\text{inv}} + P_t^{\text{imp}} - P_t^{\text{exp}} - \left(P_t^{L,\text{fix}} + P_t^{L,\text{flex}}\right) - P_t^{\text{EL}} + P_t^{\text{un}} = 0, \forall t \in \mathcal{T}. \tag{9}$$

In this equation, $P_t^{L,\text{fix}}$ and $P_t^{L,\text{flex}}$ are the fixed and shiftable loads, $P_t^{\text{EL}}$ is the AC power demand of the electrolyser, and $P_t^{\text{un}}$ is the unmet load. Together, (8) and (9) enforce instantaneous nodal power balance across the grid-connected hybrid energy system, linking the DC-side renewable and storage assets with AC-side consumption and grid transactions. Because most weak-grid systems prohibit simultaneous import and export at the point of common coupling, the model introduces a binary control variable $z_t^{\text{grid}} \in \{0, 1\}$ to enforce mutually exclusive grid directionality:

$$P_t^{\text{imp}} \le \overline{P}_{\text{gr}} \cdot z_t^{\text{grid}}, \forall t \in \mathcal{T}, \tag{10}$$

$$P_t^{\text{exp}} \le \overline{P}_{\text{gr}} \cdot \left(1 - z_t^{\text{grid}}\right), \forall t \in \mathcal{T}. \tag{11}$$

Here, $\overline{P}_{\text{gr}}$ is the contracted grid exchange limit optimised at the GA layer. These constraints guarantee compliance with grid-connection agreements and physically valid unidirectional operation at each time step. A similar logic applies to the battery subsystem, which cannot charge and discharge simultaneously. A binary variable $z_t^{\text{bat}}$ is used to indicate the operating mode (1 = discharge, 0 = charge), ensuring mutually exclusive control:

$$P_t^{\text{ch}} \le \overline{P}_{\text{ch}} \cdot \left(1 - z_t^{\text{bat}}\right), \forall t \in \mathcal{T}, \tag{12}$$



ijer, 2026, 1, Downloaded from https://onlinelibrary.wiley.com/doi/10.1155/er/5550759 by NICE, National Institute for Health and Care Excellence, Wiley Online Library on [08/11/2026]. See the Terms and Conditions (https://onlinelibrary.wiley.com/terms-and-conditions) on Wiley Online Library for rules of use; OA articles are governed by the applicable Creative Commons License

$$P_t^{\text{dis}} \le \overline{P}_{\text{dis}} \cdot z_t^{\text{bat}}, \forall t \in \mathcal{T}, \tag{13}$$

where $\overline{P}_{\text{ch}}$ and $\overline{P}_{\text{dis}}$ denote the rated charging and discharging capacities of the battery system. These constraints preserve physical realism and prevent simultaneous bidirectional energy flow within the storage subsystem. To maintain operational coherence across subsystems, the hydrogen loop is governed by a set of exclusivity and rating constraints analogous to those applied to the battery. Because the electrolyser and fuel cell connected to the same hydrogen tank, their operation must be sequential rather than simultaneous. A binary variable $z_t^{\text{H}_2} \in \{0,1\}$ determines whether hydrogen is being produced (electrolyser mode) or consumed (fuel-cell mode) at time $t$. The following constraints enforce this logic:

$$P_t^{\text{el}} \le \overline{P}_{\text{el}} \cdot \left(1 - z_t^{\text{H}_2}\right), \forall t \in \mathcal{T}, \tag{14}$$

$$P_t^{\text{fc}} \le \overline{P}_{\text{fc}} \cdot z_t^{\text{H}_2}, \forall t \in \mathcal{T}, \tag{15}$$

where $\overline{P}_{\text{el}}$ and $\overline{P}_{\text{fc}}$ represent the rated capacities of the electrolyser and fuel cell, respectively. This formulation ensures that hydrogen is never produced and consumed within the same hour, aligning the model with practical operating constraints and conversion-efficiency boundaries. The inverter throughput is constrained by its rated capacity, ensuring that the combined DC-side power converted to AC remains within technical limits:

$$P_t^{\text{inv}} \le \overline{P}_{\text{inv}}, \forall t \in \mathcal{T}. \tag{16}$$

Here, $\overline{P}_{\text{inv}}$ denotes the inverter's rated power as defined in the GA optimisation layer. This constraint enforces the system's physical conversion ceiling and links dispatch feasibility directly to design-stage inverter sizing. Since PV generation is physically located on the DC bus, the model explicitly tracks how total PV power is allocated between AC export and DC utilisation. The following equality enforces energy conservation across PV routing:

$$P_t^{\text{PV,AC}} + P_t^{\text{PV,DC}} = P_t^{\text{PV}}, \forall t \in \mathcal{T}. \tag{17}$$

Here, $P_t^{\text{PV,AC}}$and $P_t^{\text{PV,DC}}$represent the PV power routed through the inverter to the AC bus and the fraction retained on the DC side, respectively. This formulation enables the MILP to flexibly distribute generation between self-consumption, storage charging, and export, ensuring dispatch schedules remain physically consistent with the hybrid AC/DC topology.

Because the PV subsystem operates on the DC side, the model first partitions total generation between energy routed to the inverter (AC side) and energy retained within the DC domain. The DC-side component is subsequently allocated to storage charging or curtailed if capacity limits are reached. This behaviour is enforced through:

$$P_t^{\text{PV,DC}} = P_t^{\text{ch}} + P_t^{\text{cur}}, \forall t \in \mathcal{T}. \tag{18}$$

This condition ensures that all DC-directed PV output is either used for charging or curtailed, preserving nodal energy conservation. To prevent physically infeasible simultaneous charging and discharging behaviour, a binary flag $z_t^{\text{pv}} \in \{0,1\}$ is introduced to indicate PV availability on the DC bus. A "big-M" formulation is applied to activate or deactivate this logic:

$$P_t^{\text{PV,DC}} \le M_w \cdot z_t^{\text{pv}} + \varepsilon_M, \forall t \in \mathcal{T}, \tag{19}$$

$$P_t^{\text{PV,DC}} \ge \varepsilon_M \cdot z_t^{pv}, \forall t \in \mathcal{T}. \tag{20}$$

Here, $M_w$ is a horizon-specific upper bound defined as the maximum available PV power within MPC window $w$, $M_w = \max_{t \in \mathcal{T}_w} P_t^{\text{PV}}$. This bound is valid because the DC-directed PV power cannot exceed the available PV generation. Its use avoids an unnecessarily large constant and improves numerical conditioning. The tolerance $\varepsilon_M$ was set to $10^{-3}$ kW. When excess PV power at the DC side is available ($z_t^{\text{pv}} = 1$), the battery is prevented from discharging concurrently, as enforced by:

$$P_t^{\text{dis}} \le \left(1 - z_t^{\text{pv}}\right) \cdot \overline{P}_{\text{dis}}, \forall t \in \mathcal{T}. \tag{21}$$

This constraint ensures that available solar energy is prioritised for charging or direct supply before drawing from storage, thereby improving energy efficiency and reducing unnecessary cycling. The battery's state of charge (SoC) is updated at each step as a function of net charged or discharged energy, scaled by the number of modules installed and their rated capacity. The SoC evolution follows:

$$\text{SoC}_{\text{bat}}(t) = \begin{cases} \text{SoC}_{\text{init}}^{(w)}, & t = 0 \\ \text{SoC}_{\text{bat}}(t-1) + \dfrac{\eta_{\text{ch}} P_t^{\text{ch}}}{\bar{N}_{\text{bat}} B_m} - \dfrac{P_t^{\text{dis}}}{\eta_{\text{dis}} \bar{N}_{\text{bat}} B_m}, & t > 0 \end{cases}, \tag{22}$$

where $\eta_{\text{ch}}$ and $\eta_{\text{dis}}$ are the charge and discharge efficiencies, $B_m$ is the nominal capacity of a single battery module (4.8 kWh), and $\bar{N}_{\text{bat}}$ is the number of modules defined in the GA design vector. The initial SoC in each rolling window, $\text{SoC}_{\text{init}}^{(w)}$, is inherited from the previously committed interval to maintain continuity between horizons. Similarly, the hydrogen storage state, expressed as the level of hydrogen (LoH) in the tank, evolves according to the balance between electrolyser input and fuel cell output:

$$\text{LoH}(t) = \begin{cases} \text{LoH}_{\text{init}}^{(w)}, & t = 0 \\ \text{LoH}(t-1) + \dfrac{\eta_{\text{el}} P_t^{\text{EL}}}{\overline{M}_{\text{H}_2} H_{\text{LHV}}} - \dfrac{P_t^{\text{FC}}}{\eta_{\text{fc}} \overline{M}_{\text{H}_2} H_{\text{LHV}}}, & t > 0 \end{cases}. \tag{23}$$

Here, $\eta_{\text{el}}$ and $\eta_{\text{fc}}$ denote the conversion efficiencies of the electrolyser and fuel cell, $\overline{M}_{\text{H}_2}$ is the hydrogen tank capacity (kg), and $H_{\text{LHV}}$ is the lower heating value of hydrogen (kWh/kg). The initial LoH for each window, $\text{LoH}_{\text{init}}^{(w)}$, is similarly inherited from the prior window midpoint, preserving consistency across receding-horizon intervals. To capture demand-side flexibility within the predictive dispatch framework, a schedulable load is introduced representing shiftable, non-critical equipment (e.g., a swimming pool pump). This load has a fixed daily energy requirement but flexible activation timing within each 24-h horizon, allowing the optimisation to exploit periods of high renewable availability or low tariff prices. At each time step $t$, the flexible load's instantaneous power consumption is defined as:



ijer, 2026, 1, Downloaded from https://onlinelibrary.wiley.com/doi/10.1155/er/5550739 by NICE, National Institute for Health and Care Excellence, Wiley Online Library on [08/11/2026]. See the Terms and Conditions (https://onlinelibrary.wiley.com/terms-and-conditions) on Wiley Online Library for rules of use; OA articles are governed by the applicable Creative Commons License

$$P_t^{\mathrm{L,flex}} = \overline{P}_{\mathrm{flex}} \cdot z_t^{\mathrm{flex}}, \forall t \in \mathcal{T}, \tag{24}$$

where $P_t^{L,\ \mathrm{flex}}$ is the rated power of the flexible device (kW), and $z_t^{\mathrm{flex}} \in \{0,1\}$ is a binary decision variable indicating its operational status at time $t$. When $z_t^{\mathrm{flex}} = 1$, the device operates at full rated power; otherwise, its consumption is zero. This formulation enables the MILP to optimally shift flexible load operation in response to real-time economic or renewable signals. To ensure that the total energy requirement of the flexible device is met each day, a constraint enforces that it operates for a fixed number of hours $H_{\mathrm{flex}}^{\mathrm{daily}}$within every 24-h cycle. Let $\mathcal{T}_d$ denote the set of hourly time steps belonging to day $d$; the daily activation constraint is expressed as:

$$\sum_{k \in \mathcal{T}_d} z_k^{\mathrm{flex}} = H_{\mathrm{flex}}^{\mathrm{daily}}, \forall d. \tag{25}$$

This equality guarantees that the total active hours of the flexible load match its required daily operating schedule, regardless of how those hours are distributed within the day. Since the dispatch is optimised over overlapping rolling windows, each day may partially overlap multiple control horizons. To preserve temporal consistency across these overlapping windows, the model includes a memory term that tracks hours of flexible load operation already scheduled in prior segments. Let $\phi_d^{(w-1)}$denote the number of flexible load hours already executed for day $d$ in the previous window; the following constraint then enforces full-day compliance:

$$\sum_{k \in \mathcal{T}_d} z_k^{\mathrm{flex}} + \phi_d^{(w-1)} = H_{\mathrm{flex}}^{\mathrm{daily}}, \forall d. \tag{26}$$

This formulation ensures that, even as the MILP advances through receding-horizon intervals, the cumulative daily operation time remains exactly satisfied. The formulation preserves the daily energy requirement but represents an idealised upper bound on scheduling flexibility; the resulting scenarios are therefore interpreted as sensitivity cases.

## 2.3 | Case Study: Formentera Energy Community

The case study focuses on a municipal energy community situated west of Sant Francesc Xavier, the capital of Formentera Island, Spain. The cluster consists of seven public-sector buildings, including educational, administrative, and utility facilities, each with distinct load profiles and operational schedules. As shown in Figure 3, the buildings are distributed across two nearby sites and include functions such as schooling, emergency services, and public infrastructure. Their proximity and functional diversity make the site a representative testbed for decentralised energy planning, particularly under weak-grid conditions. The total annual electricity demand across the buildings is ~211 MWh, based on 2022 data provided by the Formentera Council, and serves as the baseline for evaluating the proposed optimisation framework.

## 2.4 | Grid Tariff Structure and Data Input

To evaluate cost-effectiveness under realistic regulatory and price signals, the energy system model incorporates Formentera's actual ToU electricity tariff. Figure 4a shows the community's electricity demand profile, highlighting the higher demand observed during summer. The total annual electricity consumption across all buildings is 211,665 kWh, with a daily average of 555.90 kWh, mean power demand of 23.16 kW, and a peak demand of 67.91 kW. The ToU tariff, shown in Figure 4b, is based on Endesa's six-period structure and governs both energy consumption and contracted grid capacity [29]. This data was validated through the VPP4Islands pilot project and reflects commercial billing conditions for municipal facilities [30]. The tariff feeds into a multi-component cost model comprising four billing terms:

$$C^{\mathrm{cap}} = \sum_{p=1}^{P} \overline{P}_{\mathrm{gr}} \cdot R_p \cdot D_{\mathrm{month}}, \tag{27}$$

$$C^{\mathrm{imp}} = \sum_{t \in \mathcal{T}} P_t^{\mathrm{imp}} \cdot \pi_t^{\mathrm{imp}} \Delta t, \tag{28}$$

$$C^{\mathrm{pen}} = \sum_{p=1}^{P} \tau_p \cdot 2 \cdot \left(\delta_j - 1.05 \cdot \rho_p\right), \tag{29}$$

$$R^{\mathrm{exp}} = \sum_{t \in \mathcal{T}} P_t^{\mathrm{exp}} \cdot \pi_t^{\mathrm{exp}} \Delta t, \tag{30}$$

$$O_y(x) = C_y^{\mathrm{imp}} + C_y^{\mathrm{cap}} + C_y^{\mathrm{pen}} - R_y^{\mathrm{exp}} + \sum_{t \in y} \Delta t \left(\lambda^{\mathrm{un}} P_t^{\mathrm{un}} + \lambda^{\mathrm{cur}} P_t^{\mathrm{cur}}\right). \tag{31}$$

In these equations, $\overline{P}_{\mathrm{gr}}$ and $R_p$ represent the contracted grid capacity (kW) and its corresponding price (€/kW) for each ToU period $p$, while $D_{\mathrm{month}}$ is the monthly billing duration. $P_t^{\mathrm{imp}}$and $P_t^{\mathrm{exp}}$denote the power imported from and exported to the grid at time $t$, and $\pi_t^{\mathrm{imp}}$, $\pi_t^{\mathrm{exp}}$are their respective tariffs. The penalty term incorporates measured peak load $\delta_j$, benchmarked against 105% of contracted power to reflect standard overage thresholds. The final term penalises load shedding ($P_t^{\mathrm{un}}$) and renewable curtailment ($P_t^{\mathrm{cur}}$), enforcing operational realism. Together, these cost terms form the operational cost component $O_y(\mathbf{x})$ passed to the upper-level GA for lifecycle economic evaluation.

To support accurate simulation of renewable production, solar irradiance and ambient temperature data for 2022 were retrieved from NASA's publicly available meteorological database, as illustrated by the solar irradiance in Figure 4c and ambient temperature in Figure 4d [31]. The 2022 solar resource was close to recent conditions. The modelled annual irradiation was 2153 kWh $\mathrm{m}^{-2}$, within 1% of the corresponding PVGIS value, while PVGIS and NASA POWER place 2022 within ~1.4%–1.8% of their recent multi-year means [31, 32]. Demand was less stationary: Formentera electricity consumption declined by ~10% between 2022 and 2024 [33, 34], while tourist arrivals varied from about −7% to +12% around the 2022 level [35]. These variations informed the sensitivity ranges examined below. Furthermore, the economic parameters including capital and operating costs, component lifetimes, and efficiencies, were derived from manufacturer datasheets, peer-reviewed literature, and VPP4Islands procurement data, as summarised in Table 3 [30]. They form the basis for lifecycle cost calculations and NPC assessment within the GA optimisation layer.



ijer, 2026, 1, Downloaded from https://onlinelibrary.wiley.com/doi/10.1155/er/5550739 by NICE, National Institute for Health and Care Excellence, Wiley Online Library on [08/11/2026]. See the Terms and Conditions (https://onlinelibrary.wiley.com/terms-and-conditions) on Wiley Online Library for rules of use; OA articles are governed by the applicable Creative Commons License




**FIGURE 3** | Layout of the municipal energy community west of Sant Francesc Xavier, Formentera Island. The site includes seven buildings with diverse functions and annual demands: Culture Centre (44,995 kWh), Primary School (47,189 kWh), Radio and Youth Centre (19,616 kWh), Preschool (26,596 kWh), Vehicle Inspection Station (11,486 kWh), Fire Station (23,584 kWh), and Slaughterhouse (38,199 kWh).

In addition to technical parameters, the economic assessment incorporated key financial assumptions: an 8% nominal discount rate, 2% inflation, and an electricity price escalation rate of 3% to reflect long-term market evolution. The electricity price, inclusive of tax, was taken as 5.11%, while the standard value-added tax (VAT) applied was 21%, consistent with Spanish regulatory conditions.

## 2.5 | Flexible Load Setup

Flexible demand is represented by an idealised pool-pump scheduling case. The base device is rated at 3 kW and must operate for 8 h each day, corresponding to a fixed daily energy requirement of 24 kWh. Its hourly operation is binary and may be scheduled anywhere within the day. Minimum run-time, continuity, preferred operating periods and user-comfort constraints are not represented. The 4%, 6% and 8% cases should therefore be interpreted as sensitivity cases, with the higher ratings representing aggregated or expanded shiftable equipment rather than verified demand-response programmes. Table 4 summarises the technical inputs for this flexible load, while Table 5 presents the scenarios tested to assess the effects of increased flexible load power on system efficiency and NPC. Higher-load cases (4.35 kW and 5.8 kW) emulate future expansion of load-sensitive equipment like additional pumps.

The 08:00 entry defines only the reference, unshifted operating profile. Under the MPC scenarios, the activation time is optimised freely within each day, subject to completion of the required 8 h daily operation.

## 2.6 | Uncertainty and Case-Year Sensitivity Analyses

To examine the effect of imperfect forecasts, the deterministic dispatch analysis was extended through 100 full-year Monte



ijer, 2026, 1, Downloaded from https://onlinelibrary.wiley.com/doi/10.1155/er/5550759 by NICE, National Institute for Health and Care Excellence, Wiley Online Library on [08/11/2026]. See the Terms and Conditions (https://onlinelibrary.wiley.com/terms-and-conditions) on Wiley Online Library for rules of use; OA articles are governed by the applicable Creative Commons License

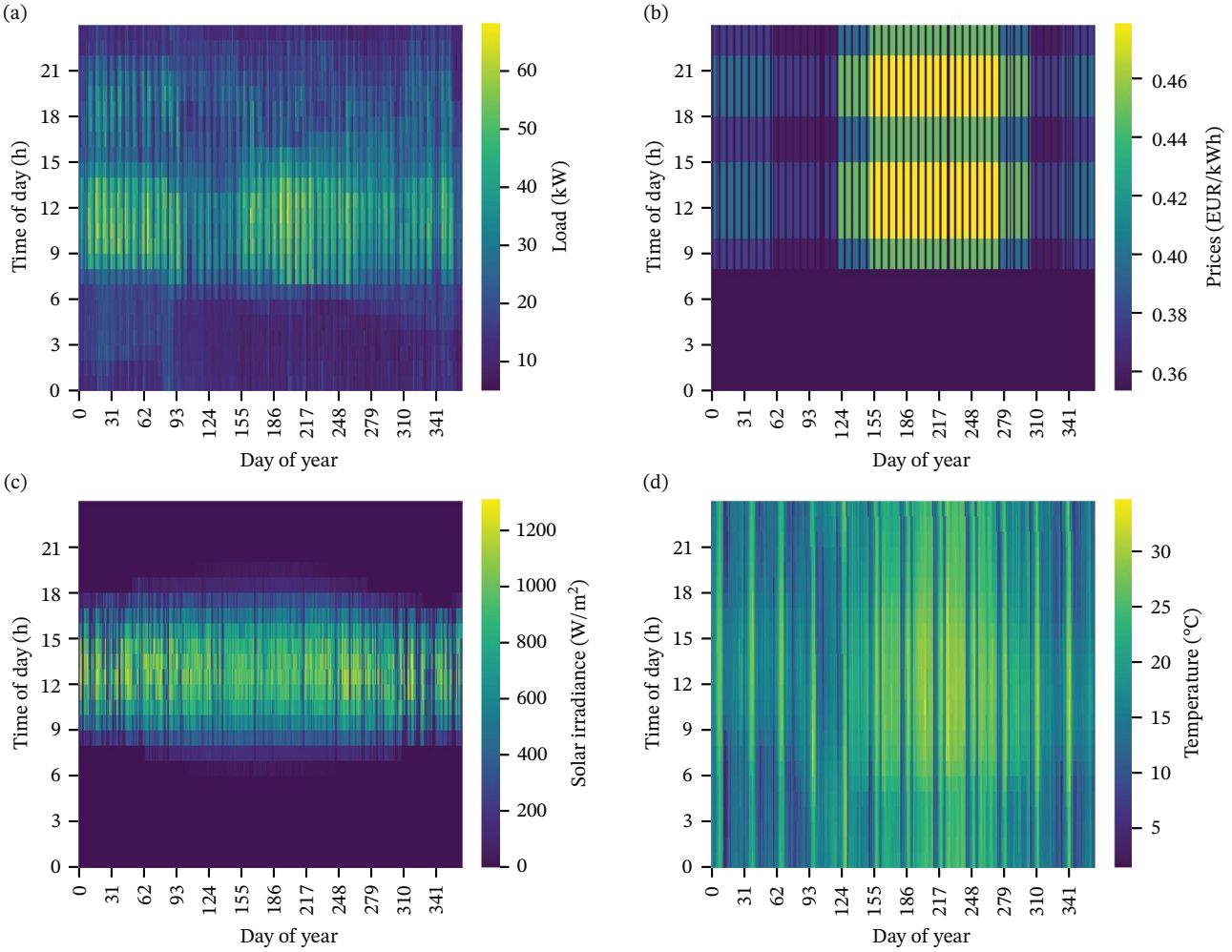



**FIGURE 4** | Data inputs for the Formentera case study: (a) community electricity demand; (b) electricity prices; (c) solar irradiance; and (d) ambient temperature.

**TABLE 3** | Techno-economic inputs for key system components, including cost, efficiency, and lifetime assumptions.

| Component | Cost | O&M | Efficiency | Lifetime |
|---|---|---|---|---|
| PV panel | €1600/kW | €10/kW·year | 20% | 25 years |
| Battery | €230/kWh | €10/kWh·year | 95% | 8000 cycles |
| Inverter | €300/kW | €10/kW·year | 96% | 20 years |
| Fuel cell | €1200/kW | €0.02/kWh | 43% | 15,000 h |
| Electrolyser | €1200/kW | €0.05/kWh | 63% | 35,000 h |
| $H_2$ tank | €500/kg | €10/kg·year | — | 15 years |

Carlo simulations. Each simulation, indexed by $s$, represents an independently generated annual forecast-error trajectory. For each hour $t$ within rolling window $\mathcal{T}_w$, the fixed-demand and irradiance forecasts were calculated as:

$$\widehat{P}_t^{L,\mathrm{fix},(s)} = P_t^{L,\mathrm{fix}}\left(1+\varepsilon_t^{L,(s)}\right),\quad \widehat{G}_t^{(s)} = G_t\left(1+\varepsilon_t^{G,(s)}\right),\quad t\in\mathcal{T}_w,\ s=1,\ldots,100. \tag{32}$$

Here, $P_t^{L,\mathrm{fix}}$ and $G_t$ are the realised fixed demand and solar irradiance already defined in the dispatch model, while $\widehat{P}_t^{L,\mathrm{fix},(s)}$ and $\widehat{G}_t^{(s)}$ are their forecast values in simulation $s$. The terms $\varepsilon_t^{L,(s)}$ and $\varepsilon_t^{G,(s)}$ denote the corresponding relative forecast errors. Forecast PV output was then calculated from $\widehat{G}_t^{(s)}$ using Equation (3). Demand and irradiance errors were sampled independently from zero-mean normal distributions limited to ±15%:

$$\varepsilon_{w,t}^{v,(s)} \sim \mathcal{N}\left(0,\sigma_{w,t}^2;[-0.15,0.15]\right),\ v\in\{L,G\}. \tag{33}$$

Here, $w$ denotes the MPC window and $s$ identifies the Monte Carlo simulation. The superscript $v$ identifies demand $(L)$ or irradiance $(G)$. Errors were sampled independently from a



ijer, 2026, 1, Downloaded from https://onlinelibrary.wiley.com/doi/10.1155/er/5550739 by NICE, National Institute for Health and Care Excellence, Wiley Online Library on [08/11/2026]. See the Terms and Conditions (https://onlinelibrary.wiley.com/terms-and-conditions) on Wiley Online Library for rules of use; OA articles are governed by the applicable Creative Commons License

**TABLE 4** | Flexible load specifications—swimming pool pump.

| Parameter | Value | Units | Description |
|---|---|---|---|
| Rated power | 3 | kW | Constant power draw during operation |
| Daily requirement | 8 | h | Must operate 8 h per day |
| Pump type | Pool | — | Non-critical, shiftable residential/commercial load |
| Operational flexibility | Full | — | Schedule adjustable within 24 h window |

**TABLE 5** | Scenarios for flexible load deployment.

| Flexible scenario (%) | Pump power (kW) | Non-flex load (kWh) | Flexible energy (kWh) | Daily runtime (h) | Base start time |
|---|---|---|---|---|---|
| 0 | 0 | 211,665 | 0 | 0 | 08:00 |
| 4 | 3 | 202,905 | 8760 | 8 | 08:00 |
| 6 | 4.35 | 198,963 | 12,702 | 8 | 08:00 |
| 8 | 5.8 | 194,729 | 16,936 | 8 | 08:00 |

zero-mean normal distribution and truncated to ±15%. Each 24-h MPC window was solved using the generated forecasts, and only the first 12 h were committed. No re-optimisation was performed after the realised demand and irradiance became known. The resulting power imbalance was expressed as:

$$\Delta P_{w,k}^{(s)} = \left(L_{w,k} - \widehat{L}_{w,k}^{(s)}\right) - \eta_{\text{inv}}\left(P_{w,k}^{\text{PV}} - \widehat{P}_{w,k}^{\text{PV},(s)}\right), \tag{34}$$

where $\Delta P_{w,k}^{(s)}$ is the realised imbalance and $\eta_{\text{inv}}$ is the inverter conversion efficiency. $P_{w,k}^{\text{PV}}$ and $\widehat{P}_{w,k}^{\text{PV},(s)}$ denote realised and forecast PV output. A positive $\Delta P$ indicates a supply deficit, whereas a negative value indicates surplus generation. These imbalances were compensated sequentially by the battery, hydrogen subsystem and grid, subject to the operating constraints defined in Equations (8)–(23). Component capacities and contracted power were held fixed throughout the analysis.

A separate fixed-design sensitivity analysis examined dependence on the 2022 case-study conditions. After deterministic sizing, the lowest-NPC configuration was held fixed and re-dispatched over the full 8760-h period under ±10% variations in solar irradiance and total demand. Import-energy and contracted-power tariff terms were varied by −30% and +10%, and a combined adverse case applied 10% lower irradiance with 10% higher demand. The controller, component capacities and ±37 kW contracted limit remained unchanged.

## 3 | Results

### 3.1 | Capacity Sizing and Economic Outcomes

This section analyses how temporal foresight and demand flexibility influence system sizing, utilisation, and grid interaction within a grid-constrained PV–battery–hydrogen community. Two comparative dimensions are examined: the decision horizon, contrasting a reactive GA–Load Following control with rolling-horizon GA–MPC, and the extent of load flexibility within the predictive framework (0–8%). Since each control strategy is embedded within its respective sizing process, the comparisons represent integrated planning outcomes; the reported differences therefore reflect the combined effects of component sizing and dispatch control rather than the isolated effect of MPC.

Table 6 summarises the principal sizing and economic outcomes for the GA–Load Following and GA–MPC configurations. The contrast in design outcomes between the two approaches illustrates how the dispatch formulation influences the resulting integrated design in weak-grid planning. Under GA–Load Following, decisions rely solely on instantaneous availability, resulting in a compact configuration: a 124 kWp PV array, 58 battery strings, a 120-kW inverter, and a contracted grid limit of 78 kW. While this minimises initial cost, it restricts internal coordination and yields a modest 227 MWh yr$^{-1}$ of PV generation, with 107 MWh yr$^{-1}$ produced outside periods of local demand. Only 56% of the load is met directly by PV, and the remaining excess is exported or converted inefficiently through under-utilised hydrogen components (electrolyser and fuel-cell capacity factors of 10% and 2%). Battery throughput remains limited at 68 MWh yr$^{-1}$, reflecting shallow cycling and reduced participation in balancing mid-day peaks. Under this integrated Load-Following design, temporal mismatch results in greater grid use for deficit and surplus management.

The corresponding annual energy balance is reported in Table 7, providing a consistent comparison of generation, direct use, storage conversion and grid exchange across the load-following and predictive-control cases.

Relative to Load Following, the MPC cases increase annual PV generation from 226.94 MWh to 274.52–283.67 MWh and reduce grid imports from 30.95 MWh to 19.83–20.74 MWh. Annual battery charging increases from 66.50 MWh to 83.74–85.07 MWh. Hydrogen conversion remains secondary, with electrolyser input of 10.37–16.01 MWh and fuel-cell output of 2.85–4.37 MWh across the MPC cases. Unmet demand remains zero and renewable curtailment is negligible in every scenario. With 24-h foresight, the optimiser expands PV capacity to 155 kWp and the battery to 76 strings while reducing the inverter rating to 77 kW and the contracted grid power to 41 kW. The result is a 25% increase in solar generation (~284 MWh yr$^{-1}$) accompanied by a one-third reduction in grid imports. Rather than simple oversizing, these changes arise from structural coupling between daily scheduling and asset sizing: batteries absorb mid-day surpluses that previously spilled to the grid, raising throughput to 84 MWh yr$^{-1}$ and stabilising depth-of-discharge profiles. Hydrogen conversion also operates proactively instead of reactively, tripling electrolyser utilisation to 30%. The system therefore extracts more value from the same solar resource, lowering external dependence while maintaining grid-compliant power flows, a central advantage for communities operating under constrained feeder capacity.

The flexible-load sensitivity cases indicate how increasing the assumed share of shiftable demand affects sizing and operation.



ijer, 2026, 1, Downloaded from https://onlinelibrary.wiley.com/doi/10.1155/er/5550759 by NICE, National Institute for Health and Care Excellence, Wiley Online Library on [08/11/2026]. See the Terms and Conditions (https://onlinelibrary.wiley.com/terms-and-conditions) on Wiley Online Library for rules of use; OA articles are governed by the applicable Creative Commons License

**TABLE 6** | System sizing and cost metrics for GA-Load following and the proposed GA–MPC configurations.

| Component | Units | GA–MPC 0% | GA–MPC 4% | GA–MPC 6% | GA–MPC 8% | GA- Load Following |
|---|---|---|---|---|---|---|
| Solar PV | kWp | 155 | 152 | 154 | 150 | 124 |
| Battery | Strings | 76 | 74 | 76 | 80 | 58 |
| Inverter | kW | 77 | 75 | 75 | 72 | 120 |
| Contracted power | kW | 41 | 40 | 39 | 37 | 78 |
| Fuel cell | kW | 5 | 5 | 5 | 5 | 5 |
| Electrolyser | kW | 6 | 5 | 5 | 5 | 5 |
| Tank | kg | 7 | 7 | 8 | 9 | 5 |
| **NPC** | € | **612,945** | **606,879** | **604,305** | **599,134** | **665,236** |
| **LCOE** | €/kWh | **0.224** | **0.221** | **0.221** | **0.218** | **0.243** |

*Note:* Bold values highlight NPC, the objective function minimised in the optimisation, and LCOE, the corresponding economic performance metric used for comparison.

**TABLE 7** | Annual energy balance for the GA-Load Following and GA–MPC scenarios.

| Component | Units | GA–MPC 0% | GA–MPC 4% | GA–MPC 6% | GA–MPC 8% | GA-Load Following |
|---|---|---|---|---|---|---|
| Annual demand | MWh $yr^{-1}$ | 211.67 | 211.67 | 211.67 | 211.67 | 211.67 |
| PV generation | MWh $yr^{-1}$ | 283.67 | 278.18 | 281.60 | 274.52 | 226.94 |
| Direct PV self-consumption | MWh $yr^{-1}$ | 123.80 | 122.56 | 122.91 | 122.62 | 119.04 |
| Renewable self-consumption | % | 43.64 | 44.05 | 43.64 | 44.67 | 52.45 |
| Battery charge | MWh $yr^{-1}$ | 83.74 | 84.30 | 84.84 | 85.07 | 66.50 |
| Battery discharge | MWh $yr^{-1}$ | 75.70 | 76.20 | 76.69 | 76.91 | 65.25 |
| Electrolyser input | MWh $yr^{-1}$ | 16.01 | 10.51 | 11.19 | 10.37 | 4.22 |
| Fuel-cell output | MWh $yr^{-1}$ | 4.37 | 2.87 | 3.07 | 2.85 | 0.99 |
| Grid import | MWh $yr^{-1}$ | 20.06 | 20.58 | 19.83 | 20.74 | 30.95 |
| Grid export | MWh $yr^{-1}$ | 59.00 | 58.28 | 60.24 | 55.10 | 30.22 |

Allowing just 4–8% of demand to shift within daily windows slightly reduces PV capacity (155 to 150 kWp) but raises battery size (76 to 80 strings) and further smooths energy flows. Flexible consumption alters the timing of demand, storage operation and grid exchange while maintaining negligible curtailment. Consequently, electrolyser and fuel-cell activity fall to 24% and 6% utilisation, signalling that internal storage and flexible loads now handle most short-term balancing. At the grid interface, contracted power tightens from 41 to 37 kW, nearly half the Load-Following requirement, while annual grid imports remain ~9%–10% of demand. These outcomes demonstrate that limited behavioural adaptation delivers disproportionate technical benefit, mitigating peak exchanges without extensive physical oversizing.

The economic implications mirror these physical adjustments. The NPC decreases from €612,945 at 0% flexibility to €599,134 at 8% flexibility, while the levelised electricity cost (LCOE) drops from €0.224 to €0.218 $kWh^{-1}$, representing a cumulative 2.25% NPC cost reduction. A modest 8% flexibility, compared to load-following, amplifies the effect reducing NPC by 9% and LCOE cost from 0.243 to 0.218 €/kWh. These improvements arise not from increased generation but from superior temporal coordination of storage and flexible demand, which suppresses both oversizing and idle losses. In summary, the GA–MPC rolling-horizon design demonstrates that limited load flexibility and inverter/grid co-optimisation can substantially improve cost-effectiveness and resilience in weak-grid community energy systems, even without major expansions of renewable capacity. The following section examines how these capacity decisions translate into real-time operational behaviour across representative winter and summer periods.

## 3.2 | Operational Dynamics: Winter and Summer Days

Seasonal operation patterns illustrate how predictive control and modest flexibility reshape internal energy flows in the PV–battery–hydrogen community under weak-grid conditions. Winter operation over 13–15 January 2022 is shown for GA–Load Following in Figure 5a and GA–MPC 8% in Figure 5b. In the GA–Load Following strategy, fixed consumption and the absence of foresight produce early-morning grid imports exceeding 100 kWh $d^{-1}$ (00:00–07:00) and abrupt midday exports during 11:00–15:00, with shallow battery cycling that limits energy autonomy. By contrast, the GA–MPC (8%) controller anticipates the limited PV generation of the second day (520 kWh $d^{-1}$) and pre-emptively shifts part of the flexible load to early hours, reducing grid import to 40–50 kWh $d^{-1}$ and avoiding the high-tariff



ijer, 2026, 1, Downloaded from https://onlinelibrary.wiley.com/doi/10.1155/er/5550739 by NICE, National Institute for Health and Care Excellence, Wiley Online Library on [08/11/2026]. See the Terms and Conditions (https://onlinelibrary.wiley.com/terms-and-conditions) on Wiley Online Library for rules of use; OA articles are governed by the applicable Creative Commons License

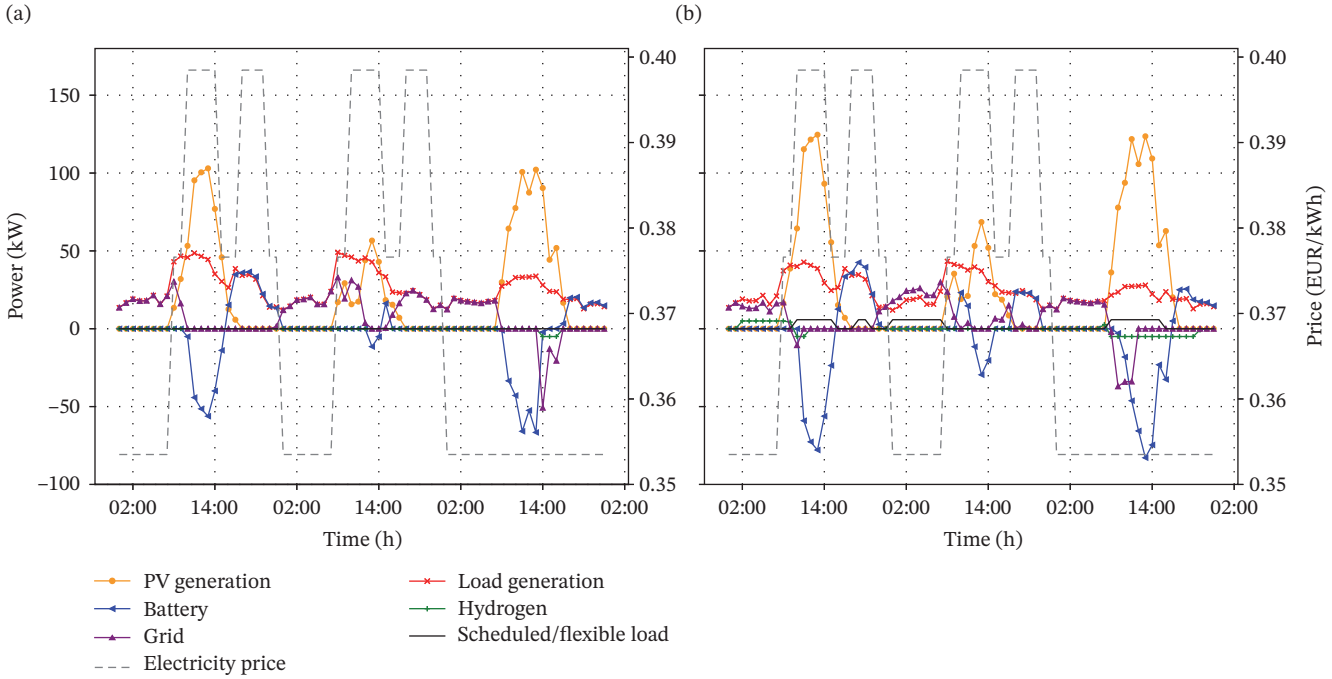



**FIGURE 5** | Winter operational dynamics for GA-Load Following (a) and the Novel GA-MPC 8% (b). The positive values for hydrogen represent the fuel cell output in kW, and the negative values indicate electrolyser consumption. For the battery, positive values indicate discharge, and negative values indicate charging. Grid interactions show positive values for electricity purchases and negative values for sales.

period. On the third day, the MPC schedule achieves smoother export behaviour, with higher battery charging peaks (80–90 kWh $d^{-1}$) and active electrolyser operation absorbing surplus energy rather than spilling it to the grid. The controller also delays early load starts on Day 1, waiting for stored energy to accumulate later in the evening (16:00–23:00). This anticipatory coordination explains the higher annual battery throughput (84 vs. 68 MWh $yr^{-1}$ in Load Following) and more consistent hydrogen utilisation, demonstrating how temporal foresight converts short-horizon optimisation into reduced grid stress and enhanced autonomy.

Figure 6a,b compare summer operation over 18–20 August 2022 under GA–Load Following and GA–MPC 8%, respectively. Daily

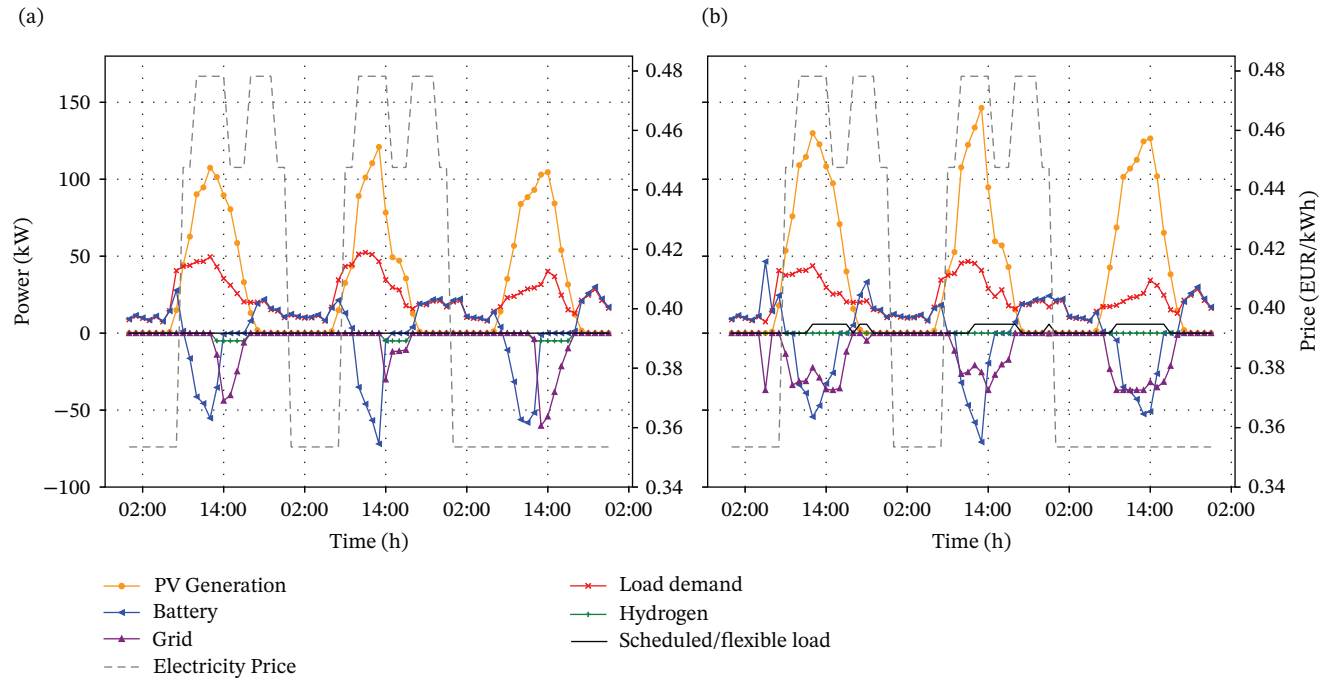



**FIGURE 6** | Summer operational dynamics for GA–Load Following (a) and the Novel GA-MPC 8% (b). The positive values for hydrogen represent the fuel cell output in kW, and the negative values indicate electrolyser consumption. For the battery, positive values indicate discharge, and negative values indicate charging. Grid interactions show positive values for electricity purchases and negative values for sales.



ijer, 2026, 1, Downloaded from https://onlinelibrary.wiley.com/doi/10.1155/er/5550759 by NICE, National Institute for Health and Care Excellence, Wiley Online Library on [08/11/2026]. See the Terms and Conditions (https://onlinelibrary.wiley.com/terms-and-conditions) on Wiley Online Library for rules of use; OA articles are governed by the applicable Creative Commons License

PV generation exceeds 570 kWh, with midday peaks (11:00–15:00) reaching 180 kW. Under GA–MPC 8% operation (Figure 6b), the controller maintains battery headroom through early-morning discharge and evening load scheduling, enabling 190–210 kWh $d^{-1}$ of midday charging and stabilised exports of 150–180 kWh $d^{-1}$. Load Following, by contrast, saturates the inverter and triggers sharp export spikes when generation exceeds local demand. The predictive controller's ability to absorb excess PV internally supports the higher installed PV capacity (150 kWp) and expanded storage system identified in Table 6. Consistent with this higher PV capacity, annual PV excess energy increases relative to Load Following (~152 vs. 108 MWh), while export also rises (about 55 vs. 30 MWh) and grid imports fall, indicating that the GA–MPC strategy captures additional value by shifting and monetising surplus rather than only increasing self-consumption.

Across the winter and summer periods, predictive coordination allows the community to internalise variability: during winter, foresight-driven scheduling prevents grid-dependent deficits; during summer, coordinated storage prevents PV overflows. These operating patterns provide the mechanistic basis for the lower contracted power and reduced NPC reported earlier, demonstrating how predictive dispatch and bounded flexibility translate fixed design capacities into measurable changes in operating cost and grid exchange. The subsequent sections examine the role of flexible demand, inverter utilisation, and grid exchange dynamics in more detail.

### 3.3 | Flexible Load Behaviour Under Price-Responsive Control

Building on the winter and summer dynamics discussed earlier, Figure 7a shows operation on 5 January, Figure 7b on 12 January, Figure 7c on 20 July and Figure 7d on July 21, 2022. The figure examines how the GA–MPC (8%) controller deploys flexibility to align electricity demand with price and renewable availability. Four representative days illustrate the contrast between winter scarcity and summer surplus conditions.

During the winter days (subplots a–b), when PV generation is limited and tariffs fluctuate between €0.35–€0.40 $kWh^{-1}$, the MPC controller consistently shifts the 8% flexible portion of the load into early morning hours (00:00–07:00). This behaviour reduces daytime grid purchases precisely when PV output is insufficient and electricity prices peak. On 12 January, for instance, 35–40 kWh of pump demand is rescheduled from 09:00–11:00 to before dawn, lowering grid imports by nearly 30% compared with a non-flexible schedule. The same foresight-driven pattern observed in Figure 5 reappears here at a finer temporal scale, anticipatory load shifting substitutes expensive midday imports with low-tariff energy, preserving the contracted power limit without compromising demand satisfaction.

In contrast, summer days (subplots c–d) show a more selective and opportunity-driven behaviour. With midday PV generation exceeding 550–580 kWh $d^{-1}$, the controller reduces unnecessary early-morning operation and concentrates the flexible load in the 08:00–10:00 window, bridging the brief period before full solar availability. On 21 July, roughly 20 kWh of demand is shifted forward to coincide with the rising PV output, ensuring that grid imports during €0.47 $kWh^{-1}$ peak hours remain negligible. This fine balancing improves internal solar utilisation and limits export volatility, supporting the smoother grid profiles identified similarly in Figure 6.

Across both representative periods, the MPC's load adaptation reflects not random demand reallocation but a cost- and foresight-driven optimisation that dynamically harmonises consumer behaviour, PV variability, and weak-grid constraints, transforming flexibility from a passive option into a structural enabler of autonomy and economic stability.

### 3.4 | Inverter Utilisation and Storage Coordination

The long-term impact of integrated control becomes clearer when viewed over the full annual cycle. Annual PV conversion and storage behaviour is presented for GA–Load Following in Figure 8a, GA–MPC 0% in Figure 8b and GA–MPC 8% in Figure 8c, linking operational dynamics directly to the sizing and cost outcomes in Table 6. In the Load-Following case, the 120 kW inverter is frequently driven to its upper limit, visibly clipping peak solar production throughout high-irradiance months. Average battery SoC stabilises near 46%, leaving insufficient headroom to absorb surpluses, while hydrogen storage remains largely idle with a mean level of only 23%. This combination explains the pronounced export excursions and the higher PV excess observed previously: PV is available during peak hours, but the system has limited capability to buffer or route that surplus beyond immediate demand.

Introducing predictive scheduling with MPC 0% modifies this behaviour. Despite a 36% smaller inverter (77 kW), the controller maintains supply adequacy by shaping state-of-charge trajectories in anticipation of midday PV availability. The battery is deliberately operated at a lower average SoC (~33%) to preserve charging headroom, while hydrogen storage rises to around 55%, providing a slower balancing buffer. These coordinated actions stabilise inverter loading and mitigate saturation-driven export excursions by allocating a greater share of PV surplus to internal storage pathways under tighter PCC operation.

When 8% flexibility is added, the MPC controller further refines this balance. The inverter rating drops again to 72 kW, yet both battery (33%) and hydrogen (51%) levels remain well regulated. Minor load shifts relieve residual PV peaks, smoothing inverter utilisation and allocating a larger fraction of midday surplus to storage and flexible demand, thereby moderating export excursions

Overall, these dynamics demonstrate that predictive control and modest flexibility enable the community to downsize power-conversion hardware while maintaining output continuity. The division of roles, with the battery providing most diurnal balancing and hydrogen offering secondary, lower-frequency support, emerges from the control logic and contributes to internal power balancing and compliance with the contracted grid-exchange limits.

### 3.5 | Grid Interaction and Contracted Power Optimisation

The transition from inverter-driven to storage-dominated coordination fundamentally reshapes the relationship between the hybrid community and the grid. Figure 9 plots the PV generation



ijer, 2026, 1, Downloaded from https://onlinelibrary.wiley.com/doi/10.1155/er/5550759 by NICE, National Institute for Health and Care Excellence, Wiley Online Library on [08/11/2026]. See the Terms and Conditions (https://onlinelibrary.wiley.com/terms-and-conditions) on Wiley Online Library for rules of use; OA articles are governed by the applicable Creative Commons License

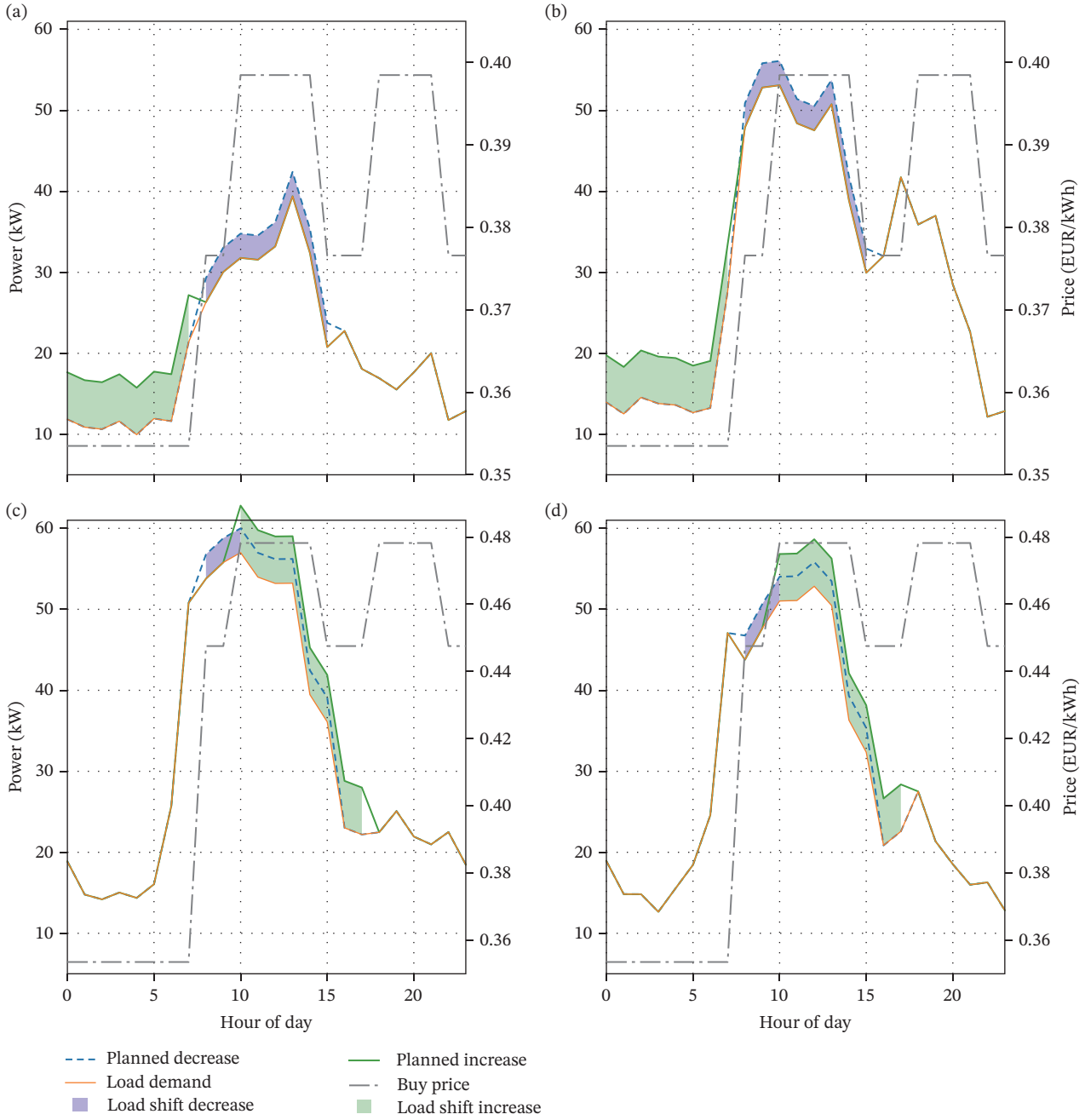



**FIGURE 7** | Hourly load profiles and pricing dynamics for MPC 8% flexible operation across four representative days: (a) 5th January 2022 and (b) 12th January 2022, representing winter days with low PV availability, whereas (c) 20th July 2022 and (d) 21st July 2022, reflecting summer days with abundant solar energy. Shaded regions indicate load shifts (green: increase, blue: decrease), highlighting MPC's adaptive strategy to minimise energy costs by aligning demand with low-tariff hours and PV generation windows. Dual-axis plots show both power demand (left *y*-axis) and electricity prices (right *y*-axis).

against grid exchange for the Load-Following and MPC 8% scenarios, directly revealing how predictive control transforms boundary behaviour.

In the Load-Following configuration (Figure 9a), operation within a ±78 kW contracted envelope produces frequent bidirectional flows. Imports persist in early-morning and low-PV conditions, while exports dominate at midday when the inverter saturates. Although grid purchases are avoided for 77% of the year, zero-import operation occurs during only 66% of hours. The distribution of points around the ±78 kW bounds shows a reactive energy pattern: surpluses and deficits are transferred almost immediately to the grid, with limited capacity for internal smoothing. This behaviour reflects the short-horizon logic of Load Following, where the grid acts as a buffer rather than a boundary.

Under GA–MPC 8% (Figure 9b), the interaction envelope narrows dramatically to ±37 kW, while the incidence of grid exchange is reduced. Grid imports fall to 14% of annual hours, and zero exchange is maintained for nearly 59% of the year. The scatter distribution flattens, with fewer excursions towards the contractual limits, indicating steadier and more internally balanced operation. This improvement arises not from overcapacity but from coordinated dispatch: flexible loads absorb short



ijer, 2026, 1, Downloaded from https://onlinelibrary.wiley.com/doi/10.1155/er/5550739 by NICE, National Institute for Health and Care Excellence, Wiley Online Library on [08/11/2026]. See the Terms and Conditions (https://onlinelibrary.wiley.com/terms-and-conditions) on Wiley Online Library for rules of use; OA articles are governed by the applicable Creative Commons License

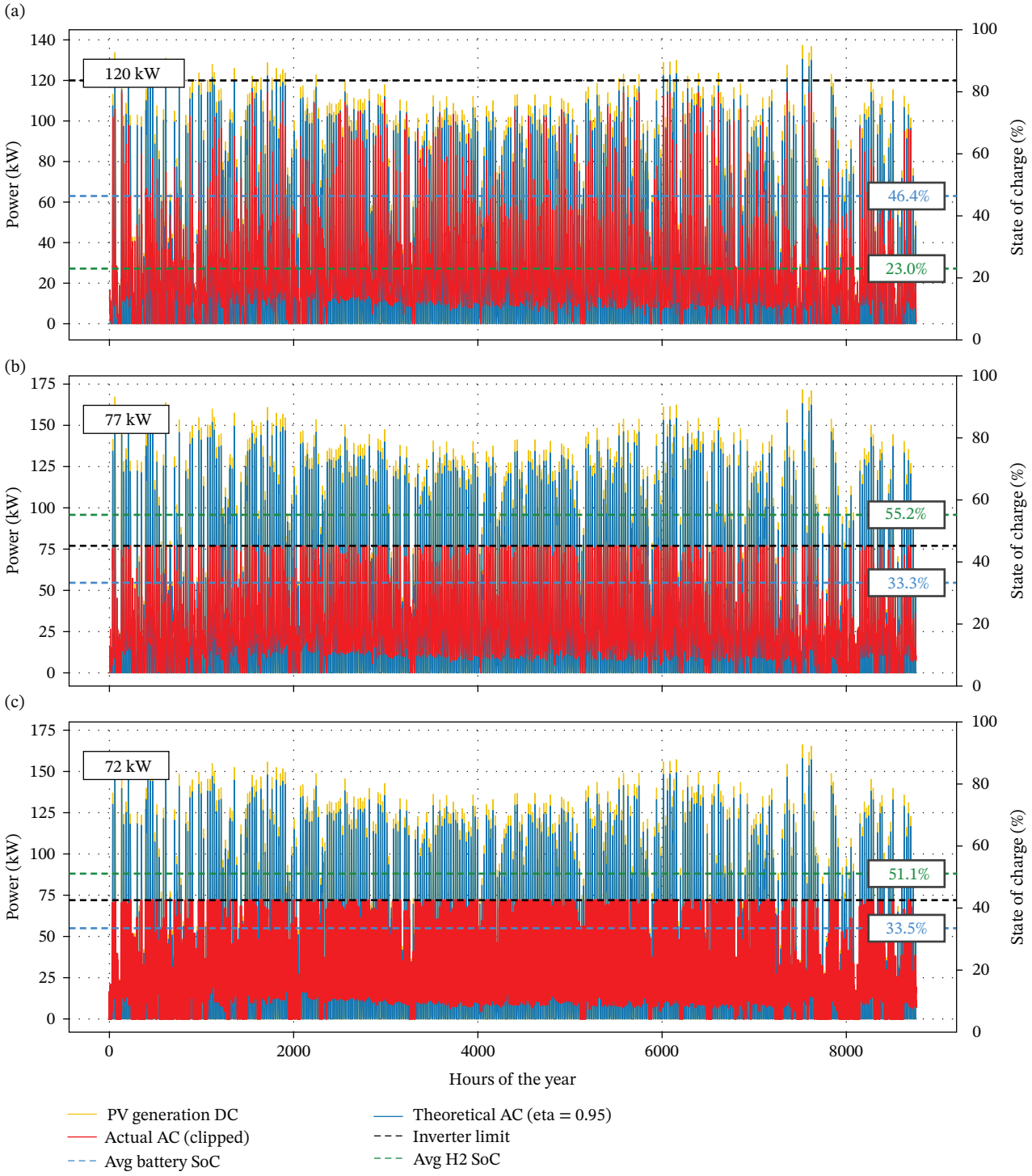



**FIGURE 8** | Annual hourly PV generation (yellow), theoretical AC (blue), and actual AC (red) outputs, together with average battery (dashed blue) and hydrogen tank (dashed green) SoC, for (a) Load-Following with a 120 kW inverter (battery ≈ 46%, $H_2$ ≈ 23%), (b) MPC 0% with a 77 kW inverter (battery ≈ 33%, $H_2$ ≈ 55%), and (c) MPC 8% with a 72 kW inverter and 8% load shifting (battery ≈ 34%, $H_2$ ≈ 51%).

surpluses, while the battery and hydrogen system provide layered discharge during deficits.

These results reinforce the mechanisms discussed. Predictive control, paired with deliberate grid and inverter co-optimisation, converts temporal foresight into structural efficiency: the community uses the grid as a contingency rather than a dependency. In weak-connection contexts, this capacity to achieve higher autonomy under tighter contractual bounds clarifies how distributed energy systems can be economically integrated while reducing peak exchanges and reliance on contracted capacity at the grid connection point.

### 3.6 | Storage Coordination and Internal Energy Balancing

The operational decisions underpinning the smoother grid behaviour in Figure 9 are illustrated in Figure 10, which tracks daily



ijer, 2026, 1, Downloaded from https://onlinelibrary.wiley.com/doi/10.1155/er/5550739 by NICE, National Institute for Health and Care Excellence, Wiley Online Library on [08/11/2026]. See the Terms and Conditions (https://onlinelibrary.wiley.com/terms-and-conditions) on Wiley Online Library for rules of use; OA articles are governed by the applicable Creative Commons License

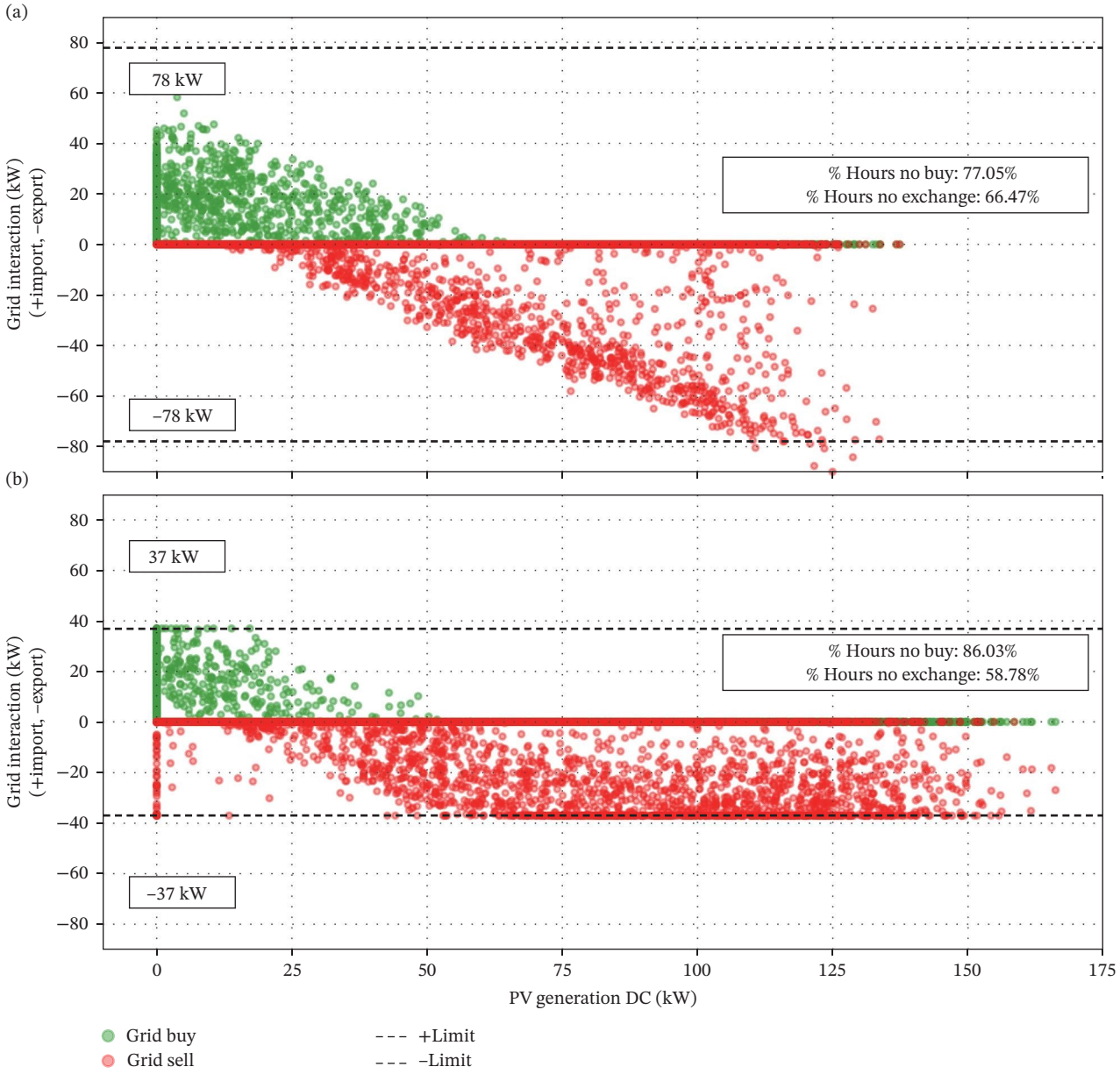



**FIGURE 9** | PV versus grid import/export for (a) Load-Following (±78 kW) and (b) MPC 8% (±37 kW): MPC achieves import-free operation 86% of hours and uses storage discharge at zero PV, flattening grid exchanges.

profiles and monthly trends of battery SoC and hydrogen LoH under Load-Following and MPC 8% operation. As each configuration uses its independently optimised component capacities, the differences reflect the combined effects of system sizing and control.

In the Load-Following configuration (Figure 10a), storage resources exhibit limited complementarity. The battery fluctuates sharply around its mid-capacity, with an annual mean SoC of 46.4%, while the hydrogen system remains largely dormant, averaging only 23% LoH. Although hydrogen inventory increases during the middle of the year, it is frequently depleted, and the battery remains the principal balancing resource. This behaviour is consistent with the inverter saturation and greater grid reliance discussed earlier.

Under MPC 8% (Figure 10b), the battery is maintained at a lower annual mean SoC of 33.5%, preserving headroom for charging, while mean hydrogen LoH increases to 51.1%. The hydrogen profile exhibits lower-frequency inventory variation, with accumulation during periods of higher PV availability followed by withdrawal later in the year. However, the 9 kg tank stores only ~300 kWh of hydrogen, equivalent to about 129 kWh of recoverable electricity at the assumed fuel-cell efficiency. The LoH profile therefore supports hydrogen's role as a complementary, lower-frequency balancing pathway.

The resulting coordination, with the battery providing diurnal smoothing and hydrogen complementing it over longer balancing intervals, supports stable inverter loading and operation within the contracted power limits. Embedding these complementary roles



ijer, 2026, 1, Downloaded from https://onlinelibrary.wiley.com/doi/10.1155/er/5550739 by NICE, National Institute for Health and Care Excellence, Wiley Online Library on [08/11/2026]. See the Terms and Conditions (https://onlinelibrary.wiley.com/terms-and-conditions) on Wiley Online Library for rules of use; OA articles are governed by the applicable Creative Commons License

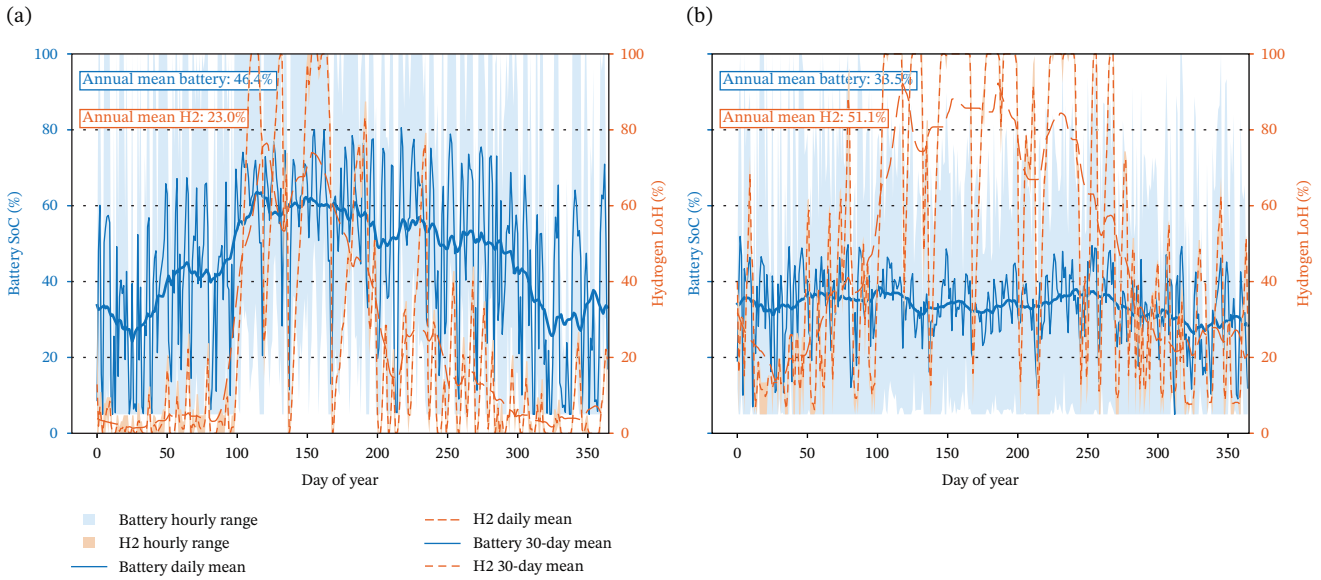



**FIGURE 10** | Annual battery SoC and hydrogen LoH under (a) Load Following and (b) MPC 8%. Each subplot shows the hourly range, daily mean and 30-day rolling average. The MPC 8% configuration operates at a lower mean battery SoC and higher mean hydrogen LoH, indicating greater use of hydrogen as a complementary balancing pathway. Shading represents hourly variation, thin lines represent daily means, and thick lines represent monthly means.

within predictive control strengthens the system's operational flexibility under weak-grid constraints.

### 3.7 | Robustness and Sensitivity Analysis

Having identified GA–MPC 8% as the preferred deterministic configuration, its robustness was evaluated using the forecast-error procedure described in Section 2.6. Table 8 reports the deterministic result together with the 5th percentile, median and 95th percentile obtained from the 100 annual simulations.

Forecast uncertainty had a limited effect on system performance. Median NPC increased by 1.57%, while the P5–P95 range corresponded to increases of 1.30%–1.85% relative to the deterministic result. Median annual grid import and export changed by −0.24% and −0.78%, respectively. Unmet demand remained zero, and grid exchange remained within the ±37 kW contracted limit in every simulation. The principal economic and grid-capacity benefits of GA–MPC 8% therefore persisted under the forecast errors examined.

A separate fixed-design analysis examined sensitivity to the case-year assumptions. The GA–MPC 8% configuration was re-dispatched under the resource, demand and tariff variations defined in Section 2.6. Table 9 reports changes relative to the corresponding 2022 re-dispatch baseline.

The fixed configuration remained operationally feasible throughout the tested range. A 10% reduction in irradiance increased NPC and LCOE by 7.89%, whereas a 10% increase reduced both metrics by 4.17%. Demand variation had a greater effect on NPC than on LCOE because the latter is normalised by annual electricity demand. The tariff-only cases mainly affected the economic indicators: reducing tariff levels by 30% lowered NPC and LCOE by 8.17%, whereas increasing tariffs by 10% raised both by 2.54%; annual grid import and export changed only marginally because the component capacities, dispatch logic and ±37 kW contracted-power limit were kept fixed. In the combined adverse case, with 10% lower irradiance and 10% higher demand, NPC and LCOE increased by 20.12% and 9.20%, respectively. Nevertheless, unmet demand remained zero and the ±37 kW contracted limit was maintained. The selected configuration therefore remained feasible beyond the exact 2022 inputs examined, although the findings remain site-specific and economic performance depends on local resource, demand and tariff conditions.

The results are consistent with earlier evidence that incorporating look-ahead dispatch within sizing can reduce lifecycle cost. Mohseni and Brent [15] reported savings of up to 8% when extending battery scheduling to 72 h, while the present framework reduces NPC by ~9% relative to GA–Load Following. Unlike the earlier formulations reviewed, the present analysis

**TABLE 8** | Forecast-error sensitivity of the GA–MPC 8% configuration.

| Component | Units | Deterministic result | MC P5 | MC median | MC P95 | Median change (%) |
|---|---|---|---|---|---|---|
| NPC | € | 599,134 | 606,920 | 608,540 | 610,230 | 1.57 |
| Grid import | MWh | 20.74 | 20.58 | 20.69 | 20.81 | −0.24 |
| Grid export | MWh | 55.10 | 54.45 | 54.67 | 54.86 | −0.78 |



ijer, 2026, 1, Downloaded from https://onlinelibrary.wiley.com/doi/10.1155/er/5550759 by NICE, National Institute for Health and Care Excellence, Wiley Online Library on [08/11/2026]. See the Terms and Conditions (https://onlinelibrary.wiley.com/terms-and-conditions) on Wiley Online Library for rules of use; OA articles are governed by the applicable Creative Commons License

**TABLE 9** | Sensitivity of the fixed GA–MPC 8% configuration to case-year assumptions.

| Scenario | NPC change (%) | LCOE change (%) | Grid import (MWh) | Grid export (MWh) |
|---|---|---|---|---|
| 2022 Reference | 0 | 0 | 20.74 | 55.1 |
| Solar −10% | 7.89 | 7.89 | 26.58 | 35.67 |
| Solar +10% | −4.17 | −4.17 | 17.57 | 75.09 |
| Demand −10% | −7.86 | 2.37 | 15.11 | 70.65 |
| Demand +10% | 10.12 | 0.11 | 28.32 | 41.07 |
| Tariff −30% | −8.17 | −8.17 | 20.72 | 55.07 |
| Tariff +10% | 2.54 | 2.54 | 20.69 | 55.03 |
| Combined adverse | 20.12 | 9.2 | 37.27 | 25.44 |

also co-optimises inverter rating and contracted grid capacity, reducing the latter from ±78 to ±37 kW. Direct numerical comparison remains conditional on differences in system scale, tariffs and resource profiles.

## 4 | Conclusion

The results reframe what "optimal sizing" means for weak-grid energy communities. When import and export capacity at the grid connection point is treated as a binding design constraint, the central problem shifts from maximising annual renewable energy use to shaping short-horizon power trajectories so that autonomy is achieved within an enforceable exchange envelope. The novelty of the proposed GA–MILP–MPC architecture is therefore not the use of optimisation per se, but the way it couples long-horizon investment decisions to a dispatch model that explicitly internalises tariff signals, inverter throughput limits, and contracted power as co-determined quantities. In doing so, it closes a common modelling gap where the grid is implicitly treated as a limitless sink and source, and where feasibility at the boundary is checked after sizing rather than used to define value during sizing.

Across the case study, predictive dispatch converts temporal foresight into structural efficiency at the interface. Compared with GA–Load Following, the selected GA–MPC 8% configuration reduces contracted grid capacity from ±78 to ±37 kW and inverter rating from 120 to 72 kW. NPC decreases from €665,236 to €599,134 and LCOE from 0.243 to 0.218 €/kWh. Annual grid imports fall from 30.95 to 20.74 MWh and unmet demand remains zero. The same installed energy resources deliver different system value depending on whether they are operated to preserve headroom, avoid conversion bottlenecks, and pre-empt expensive or capacity-limited exchanges. This is why the solutions that tighten the contracted envelope do not simply compensate by leaning harder on the grid; instead they reorganise internal roles so that the battery is positioned for diurnal smoothing while hydrogen provides complementary support over longer balancing intervals, with modest load shifting acting as a final degree of freedom that trims residual peaks rather than driving the outcome on its own. The consistent pattern is that boundary compliance becomes an operational objective that shapes investment, rather than an operational inconvenience managed by curtailment or exports.

For planning, this implies that the economic case for hybrid battery–hydrogen systems on constrained feeders is anchored in their ability to substitute internal flexibility for contracted capacity and oversized power conversion, while keeping tariff exposure and exchange volatility low. The forecast-error analysis confirmed that the principal benefits persisted under demand and irradiance errors bounded at ±15%. Across 100 full-year simulations, unmet demand remained zero, the ±37 kW contracted limit was maintained, and median NPC increased by only 1.57% relative to the deterministic case. Fixed-design sensitivity tests similarly maintained zero unmet demand and compliance with the ±37 kW limit across the examined solar, demand and tariff variations, including the combined 10% irradiance reduction and 10% demand increase. Future work should extend the analysis to multi-year and multi-site datasets, correlated forecast errors, alternative export remuneration and component ageing.

**Nomenclature**

| | |
|---|---|
| AC: | Alternating current |
| AD: | Detailed AC/DC bus representation |
| BESS: | Battery energy storage system |
| BT: | Battery storage |
| CG: | Contracted-grid capacity optimisation |
| DC: | Direct current |
| DG: | Diesel generator |
| DO: | Dispatch optimisation |
| EL: | Electrolyser |
| EMPC: | Economic model predictive control |
| FC: | Fuel cell |
| GA: | Genetic algorithm |
| INV: | Inverter |
| LCOE: | Levelised cost of electricity |
| LHV: | Lower heating value |
| LoH: | Level of hydrogen |
| LS: | Load shifting |
| MC: | Monte Carlo |



ijer, 2026, 1, Downloaded from https://onlinelibrary.wiley.com/doi/10.1155/er/5550739 by NICE, National Institute for Health and Care Excellence, Wiley Online Library on [08/11/2026]. See the Terms and Conditions (https://onlinelibrary.wiley.com/terms-and-conditions) on Wiley Online Library for rules of use; OA articles are governed by the applicable Creative Commons License

| | |
|---|---|
| MILP: | Mixed-integer linear programming |
| MPC: | Model predictive control |
| NPC: | Net present cost |
| O&M: | Operation and maintenance |
| P5, P95: | Fifth and ninety-fifth percentiles |
| PCC: | Point of common coupling |
| PS: | Peak shaving |
| PV: | Photovoltaic |
| RH: | Rolling horizon |
| SoC: | State of charge |
| STC: | Standard test conditions |
| TK: | Hydrogen storage tank |
| TN: | Truncated normal distribution |
| ToU: | Time-of-use |
| VPP: | Virtual power plant |

**Symbols**

| | |
|---|---|
| $t$: | Hourly dispatch time index |
| $w$: | Rolling-horizon MPC window index |
| $d$: | Day index |
| $k$: | System-component index |
| $y$: | Project-year index |
| $p$: | ToU tariff-period index |
| $s$: | Monte Carlo simulation index |
| $x$: | Forecast-error source identifier, with $x$ in {L,G} |
| $Y$: | Project lifetime (year) |
| $P$: | Number of ToU tariff periods |
| $\mathcal{X}$: | Feasible design space |
| $\mathcal{K}$: | Set of system components |
| $\mathcal{T}$: | Complete set of dispatch time steps |
| $T_w$: | Set of hourly time steps in MPC window w |
| $T_d$: | Set of hourly time steps belonging to day d |
| $\Delta t$: | Dispatch time-step duration (h) |
| $x$: | GA design vector |
| $\overline{P}_{pv}$: | Installed PV capacity (kWp) |
| $\overline{N}_{\mathrm{bat}}$: | Number of installed battery modules (module) |
| $\overline{P}_{\mathrm{inv}}$: | Rated inverter power (kW) |
| $\overline{P}_{\mathrm{gr}}$: | Contracted grid import/export power limit (kW) |
| $\overline{P}_{\mathrm{fc}}$: | Rated fuel-cell power (kW) |
| $\overline{P}_{\mathrm{el}}$: | Rated electrolyser power (kW) |
| $\overline{M}_{\mathrm{H_2}}$: | Hydrogen-tank capacity (kg) |
| $\mathrm{NPC}(x)$: | Net present cost of design $x$ (EUR) |
| $C_{(k,y)}(x)$: | Capital cost of component $k$ in year $y$ (EUR) |
| $R_{(k,y)}(x)$: | Replacement cost of component $k$ in year $y$ (EUR) |
| $S_{(k,y)}(x)$: | Salvage value of component $k$ in year $y$ (EUR) |
| $O_y(x)$: | Operating cost in year $y$ (EUR $\mathrm{yr}^{-1}$) |
| $i$: | Real discount rate |
| $\Phi$: | Annual energy-imbalance penalty added to the GA objective (EUR) |
| $\Phi_{\mathrm{ex/un}}$: | Penalty applied when annual excess or unmet energy exceeds its tolerance (EUR) |
| $E_{\mathrm{ex/un}}$: | Cumulative annual excess or unmet energy (kWh $\mathrm{yr}^{-1}$) |
| $\varepsilon_E$: | Annual energy-imbalance tolerance (kWh $\mathrm{yr}^{-1}$) |
| $\pi_t^{\mathrm{imp}}$: | Grid-import energy tariff at time $t$ (EUR $\mathrm{kWh}^{-1}$) |
| $\pi_t^{\mathrm{exp}}$: | Grid-export remuneration at time $t$ (EUR $\mathrm{kWh}^{-1}$) |
| $\lambda_{\mathrm{un}}$: | Unmet-load penalty coefficient (EUR $\mathrm{kWh}^{-1}$) |
| $\lambda_{\mathrm{cur}}$: | Renewable-curtailment penalty coefficient (EUR $\mathrm{kWh}^{-1}$) |
| $C^{\mathrm{cap}}$: | Contracted-capacity charge (EUR) |
| $C^{\mathrm{imp}}$: | Grid-import energy cost (EUR) |
| $C^{\mathrm{pen}}$: | Contracted-power exceedance penalty (EUR) |
| $R^{\mathrm{exp}}$: | Grid-export revenue (EUR) |
| $R_p$: | Contracted-capacity tariff in ToU period p (EUR $\mathrm{kW}^{-1}$ $\mathrm{period}^{-1}$) |
| $D_{\mathrm{month}}$: | Billing duration represented in the capacity charge (month) |
| $\tau_p$: | Power-exceedance penalty rate in ToU period p (EUR $\mathrm{kW}^{-1}$) |
| $\delta_p$: | Measured maximum grid power in ToU period p (kW) |
| $P_t^{\mathrm{PV}}$: | Available PV power at time $t$ (kW) |
| $\eta_{\mathrm{der}}$: | PV derating factor |
| $G_t$: | Incident solar irradiance at time $t$ (kW . $\mathrm{m}^{-2}$) |
| $G_{(\mathrm{STC})}$: | Solar irradiance under STC (kW $\mathrm{m}^{-2}$) |
| $\alpha$: | PV temperature coefficient (degree C $^{-1}$) |
| $T_t$: | PV-cell temperature at time $t$ (degree C) |
| $T_{(\mathrm{STC})}$: | PV-cell temperature under STC (degree C) |
| $P_t^{\mathrm{PV,AC}}$: | PV power routed towards the AC bus (kW) |
| $P_t^{\mathrm{PV,DC}}$: | PV power retained on the DC bus (kW) |
| $P_t^{\mathrm{inv}}$: | DC-to-AC inverter throughput (kW) |
| $\eta_{\mathrm{inv}}$: | Inverter conversion efficiency |
| $P_t^{\mathrm{imp}}$: | Grid-import power (kW) |
| $P_t^{\mathrm{exp}}$: | Grid-export power (kW) |
| $P_t^{L,\mathrm{fix}}$: | Fixed electrical demand (kW) |
| $P_t^{L,\mathrm{flex}}$: | Flexible electrical demand (kW) |
| $P_t^{\mathrm{un}}$: | Unmet electrical demand (kW) |
| $P_t^{\mathrm{cur}}$: | Curtailed renewable power (kW) |
| $P_t^{\mathrm{ch}}$: | Battery charging power (kW) |
| $P_t^{\mathrm{dis}}$: | Battery discharging power (kW) |
| $\overline{P}_{\mathrm{ch}}$: | Rated battery charging power (kW) |
| $\overline{P}_{\mathrm{dis}}$: | Rated battery discharging power (kW) |
| $z_t^{\mathrm{bat}}$: | Battery operating-mode variable: 1 for discharge and 0 for charge (binary) |
| $\mathrm{SoC}_{\mathrm{bat}}(t)$: | Battery state of charge (p.u.) |
| $\mathrm{SoC}_{\mathrm{init}}(w)$: | Battery SoC at the start of MPC window w (p.u.) |
| $\eta_{\mathrm{ch}}$: | Battery charging efficiency |
| $\eta_{\mathrm{dis}}$: | Battery discharging efficiency |



ijer, 2026, 1, Downloaded from https://onlinelibrary.wiley.com/doi/10.1155/er/5550739 by NICE, National Institute for Health and Care Excellence, Wiley Online Library on [08/11/2026]. See the Terms and Conditions (https://onlinelibrary.wiley.com/terms-and-conditions) on Wiley Online Library for rules of use; OA articles are governed by the applicable Creative Commons License

| | |
|---|---|
| $B_m$: | Nominal capacity of one battery module (kWh module$^{-1}$) |
| $P_t^{\mathrm{EL}}$: | Electrolyser electrical input power (kW) |
| $P_t^{\mathrm{FC}}$: | Fuel-cell electrical output power (kW) |
| $z_t^{\mathrm{H_2}}$: | Hydrogen operating-mode variable: 1 for fuel-cell mode and 0 for electrolyser mode (binary) |
| $\mathrm{LoH}(t)$: | Hydrogen inventory as a fraction of tank capacity (p.u.) |
| $\mathrm{LoH}_{\mathrm{init}}(w)$: | Hydrogen inventory at the start of MPC window w (p.u.) |
| $\eta_{\mathrm{el}}$: | Electrolyser conversion efficiency |
| $\eta_{\mathrm{fc}}$: | Fuel-cell conversion efficiency |
| $H_{\mathrm{LHV}}$: | Lower heating value of hydrogen (kWh kg$^{-1}$) |
| $z_t^{\mathrm{grid}}$: | Grid-direction variable: 1 for import and 0 for export (binary) |
| $z_t^{\mathrm{pv}}$: | PV-availability flag for DC-side charging logic (binary) |
| $M_w$: | Big-M constant used in the PV/battery logic (kW) |
| $\varepsilon_M$: | Small positive numerical tolerance (kW) |
| $\overline{P}_{\mathrm{flex}}$: | Rated power of the flexible device (kW) |
| $z_t^{\mathrm{flex}}$: | Flexible-device operating status (binary) |
| $H_{\mathrm{flex}}^{\mathrm{daily}}$: | Required daily operating duration of the flexible device (h day$^{-1}$) |
| $\psi_d^{(w-1)}$: | Flexible-load operating hours already committed for day d before window w (h) |
| $\overline{P}_t^{L,\mathrm{fix},(s)}$: | Fixed-demand forecast at time $t$ in simulation s (kW) |
| $\overline{G}_t^{(s)}$: | Irradiance forecast at time $t$ in simulation $s$ (kW m$^{-2}$) |
| $\varepsilon_t^{(x,(s))}$: | Relative forecast error for quantity $x$ at time $t$ in simulation $s$ |
| $\sigma_t$: | Standard deviation assigned to the relative forecast error at time $t$ |
| $(0, \sigma_t^2; -0.15, 0.15)$: | Zero-mean normal distribution truncated to the interval [−0.15, 0.15] |
| $\overline{P}_t^{\mathrm{PV},(s)}$: | PV-power forecast at time $t$ in simulation $s$ (kW) |
| $\Delta P_t^{(s)}$: | Realised power imbalance in simulation $s$; positive for deficit and negative for surplus (kW). |


## Acknowledgments

The authors would like to acknowledge funding received from the European Union's Horizon 2020 Research and Innovation Programme for the VPP4Islands project (Virtual Power Plant for Interoperable and Smart isLANDS) under grant number 957852.

## Funding

The study was funded by the European Union's Horizon 2020 Research and Innovation Programme for the VPP4Islands project (Virtual Power Plant for Interoperable and Smart isLANDS) (Grant 957852).



## Disclosure

For the purposes of open access, the author has applied a Creative Commons Attribution (CC BY) Licence to any Accepted Author Manuscript version arising from this submission.


## Conflicts of Interest

The authors declare no conflicts of interest.

## Data Availability Statement

The data that support the findings of this study are available upon request from the corresponding author. The data are not publicly available due to privacy or ethical restrictions.

## References


1. Y. Chen, B. Dai, W. Ren, H. Niu, and Z. Chen, "A Comprehensive Review of Energy Security in Islanded Regions: Challenges, Strategies, and Sustainable Development Pathways," *Renewable and Sustainable Energy Reviews* 220 (2025): 115879.

2. Directorate-General for Energy, "In Focus: EU Islands and the Clean Energy Transition," (European Commission, 2021).

3. E. Bertoli, S. Laera, and F. van Dedem, "Islands Need Resilient Power Systems More Than Ever: Clean Energy Can Deliver," (International Energy Agency (IEA), 2024), Accessed on September 4, 2024 https://www.iea.org/commentaries/islands-need-resilient-power-systems-more-than-ever-clean-energy-can-deliver.

4. A. Papadaki, N. Savvakis, N. Sifakis, and G. Arampatzis, "Analysis of Hybrid Renewable Energy Systems for European Islands: Market Dynamics, Opportunities and Challenges," *Sustainable Futures* 9 (2025): 100601.

5. G. N. Psarros and S. A. Papathanassiou, "Generation Scheduling in Island Systems With Variable Renewable Energy Sources: A Literature Review," *Renewable Energy* 205 (2023): 1105–1124.

6. Á. Ordóñez, E. Sánchez, J. Carlos Solano, and J. Parra-Domínguez, "Demand Charges Reduction With Photovoltaics in Industry," *Heliyon* 10, no. 1 (2024): e23404.

7. L. Ge, B. Zhang, W. Huang, et al., "A Review of Hydrogen Generation, Storage, and Applications in Power System," *Journal of Energy Storage* 75 (2024): 109307.

8. Y. He, S. Guo, P. Dong, Y. Zhang, J. Huang, and J. Zhou, "A State-of-the-Art Review and Bibliometric Analysis on the Sizing Optimization of Off-Grid Hybrid Renewable Energy Systems," *Renewable and Sustainable Energy Reviews* 183 (2023): 113476.

9. A. J. Handique, R. A. M. Peer, and J. Haas, "Understanding the Challenges for Modelling Islands' Energy Systems and How to Solve Them," *Current Sustainable/Renewable Energy Reports* 11, no. 4 (2024): 95–104.

10. L. P. Van, K. D. Chi, and T. N. Duc, "Review of Hydrogen Technologies Based Microgrid: Energy Management Systems, Challenges and Future Recommendations," *International Journal of Hydrogen Energy* 48, no. 38 (2023): 14127–14148.

11. B. Modu, M. P. Abdullah, A. L. Bukar, and M. F. Hamza, "A Systematic Review of Hybrid Renewable Energy Systems With Hydrogen Storage: Sizing, Optimization, and Energy Management Strategy," *International Journal of Hydrogen Energy* 48, no. 97 (2023): 38354–38373.

12. Y. Zhang, P. E. Campana, A. Lundblad, and J. Yan, "Comparative Study of Hydrogen Storage and Battery Storage in Grid Connected Photovoltaic System: Storage Sizing and Rule-Based Operation," *Applied Energy* 201 (2017): 397–411.

13. P. Gabrielli, M. Gazzani, E. Martelli, and M. Mazzotti, "Optimal Design of Multi-Energy Systems With Seasonal Storage," *Applied Energy* 219 (2018): 408–424.

14. P. Rullo, L. Braccia, P. Luppi, D. Zumoffen, and D. Feroldi, "Integration of Sizing and Energy Management Based on Economic Predictive Control for Standalone Hybrid Renewable Energy Systems," *Renewable Energy* 140 (2019): 436–451.

15. S. Mohseni and A. C. Brent, "A Metaheuristic-Based Micro-Grid Sizing Model With Integrated Arbitrage-Aware Multi-Day Battery Dispatching," *Sustainability* 14, no. 19 (2022): 12941.





ijer, 2026, 1, Downloaded from https://onlinelibrary.wiley.com/doi/10.1155/er/5550759 by NICE, National Institute for Health and Care Excellence, Wiley Online Library on [08/11/2026]. See the Terms and Conditions (https://onlinelibrary.wiley.com/terms-and-conditions) on Wiley Online Library for rules of use; OA articles are governed by the applicable Creative Commons License

16. A. Al-Quraan and B. Al-Mhairat, "Sizing and Energy Management of Grid-Connected Hybrid Renewable Energy Systems Based on Techno-Economic Predictive Technique," *Renewable Energy* 228 (2024): 120639.

17. F. A. Kassab, B. Celik, F. Locment, M. Sechilariu, S. Liaquat, and T. M. Hansen, "Optimal Sizing and Energy Management of a Microgrid: A Joint MILP Approach for Minimization of Energy Cost and Carbon Emission," *Renewable Energy* 224 (2024): 120186.

18. S. Singh, P. Chauhan, and N. J. Singh, "Capacity Optimization of Grid Connected Solar/Fuel Cell Energy System Using Hybrid ABC-PSO Algorithm," *International Journal of Hydrogen Energy* 45, no. 16 (2020): 10070–10088.

19. O. Talent and H. Du, "Optimal Sizing and Energy Scheduling of Photovoltaic-Battery Systems Under Different Tariff Structures," *Renewable Energy* 129 (2018): 513–526.

20. T. Kaewnukultorn, S. B. Sepúlveda-Mora, and S. Hegedus, "The Impacts of DC/AC Ratio, Battery Dispatch, and Degradation on Financial Evaluation of Bifacial PV+BESS Systems," *Renewable Energy* 236 (2024): 121402.

21. B. Modu, M. P. Abdullah, A. AlKassem, M. F. Hamza, and A. L. Bukar, "The Role of Hybrid Hydrogen-Battery Storage in a Grid-Connected Renewable Energy Microgrid Considering Time-of-Use Electricity Tariffs," *Journal of Energy Storage* 105 (2025): 114729.

22. J. Li, J. Zhao, Y. Chen, L. Mao, K. Qu, and F. Li, "Optimal Sizing for a Wind-Photovoltaic-Hydrogen Hybrid System Considering Levelized Cost of Storage and Source-Load Interaction," *International Journal of Hydrogen Energy* 48, no. 11 (2023): 4129–4142.

23. M. A. Gelchu, J. Ehnberg, D. Shiferaw, and E. O. Ahlgren, "Impact of Demand-Side Management on the Sizing of Autonomous Solar PV-Based Mini-Grids," *Energy* 278 (2023): 127884.

24. A. Mehrabani, H. Allah Aalami, and A. Pirayesh Neghab, "Integrated Planning Framework for Microgrid Incorporating the Flexibility Provision Capabilities of Demand Response Programs," *International Journal of Electrical Power & Energy Systems* 155 (2024): 109521.

25. P. Marocco, D. Ferrero, E. Martelli, M. Santarelli, and A. Lanzini, "An MILP Approach for the Optimal Design of Renewable Battery-Hydrogen Energy Systems for Off-Grid Insular Communities," *Energy Conversion and Management* 245 (2021): 114564.

26. S. Mohseni, A. C. Brent, and D. Burmester, "A Demand Response-Centred Approach to the Long-Term Equipment Capacity Planning of Grid-Independent Micro-Grids Optimized by the Moth-Flame Optimization Algorithm," *Energy Conversion and Management* 200 (2019): 112105.

27. P. Marocco, M. Gandiglio, and M. Santarelli, "Optimal Design of PV-Based Grid-Connected Hydrogen Production Systems," *Journal of Cleaner Production* 434 (2024): 140007.

28. T. S. Le, T. N. Nguyen, D.-K. Bui, and T. D. Ngo, "Optimal Sizing of Renewable Energy Storage: A Techno-Economic Analysis of Hydrogen, Battery and Hybrid Systems Considering Degradation and Seasonal Storage," *Applied Energy* 336 (2023): 120817.

29. Endesa, "Electricity Access Tariffs for Businesses," (Endesa, 2024), Accessed on August 6, 2024 https://www.endesa.com/en/companies/electricity-access-tariffs-for-businesses.

30. VPP4ISLANDS, "VPP4ISLANDS: Virtual Power Plant for Interoperable and Smart isLANDS," 2023, Accessed on June 14, 2023 https://vpp4islands.eu/.

31. National Aeronautics and Space Administration (NASA), "NASA Prediction of Worldwide Energy Resources (POWER) Data Access Viewer," (NASA Langley Research Center, 2024), Accessed on August 6, 2024 https://power.larc.nasa.gov/data-access-viewer/.

32. European Commission, Joint Research Centre (JRC), "Photovoltaic Geographical Information System (PVGIS)," (European Commission, 2026), Accessed on June 14, 2026 https://re.jrc.ec.europa.eu/pvg_tools/en/.

33. Europa Press, "La demanda eléctrica crece un 10,3% en Baleares durante 2022, según Endesa," (Europa Press, 2023), Accessed on June 14, 2026 https://www.europapress.es/illes-balears/noticia-demanda-electrica-crece-103-baleares-2022-endesa-20230109115958.html.

34. Europa Press, "La demanda eléctrica en Baleares aumenta un 0,5% en 2024," (Europa Press, 2024), Accessed on June 14, 2026 https://www.europapress.es/illes-balears/noticia-demanda-electrica-baleares-aumenta-05-2024-20250109131910.html.

35. Instituto de Estadística de las Illes Balears (IBESTAT), "Turistes amb destinació principal Eivissa i Formentera per període, país de residència i illa de destinació. Des de 2019T1 a 2025T2," 2025, Accessed on June 14, 2026 https://datos.gob.es/es/catalogo/a04027063-turistas-con-destino-principal-eivissa-y-formentera-por-periodo-pais-de-residencia-e-isla-de-destino-desde-2019t1-a-2025t2-illes-balears.



ijer, 2026, 1, Downloaded from https://onlinelibrary.wiley.com/doi/10.1155/er/5550739 by NICE, National Institute for Health and Care Excellence, Wiley Online Library on [08/11/2026]. See the Terms and Conditions (https://onlinelibrary.wiley.com/terms-and-conditions) on Wiley Online Library for rules of use; OA articles are governed by the applicable Creative Commons License